THE ASTROPHYSICAL JOURNAL, 405:567–583, 1993 March 10

THE ELEMENTAL AND ISOTOPIC COMPOSITION OF GALACTIC COSMIC-RAY NUCLEI FROM SCANDIUM THROUGH NICKEL[1]

RICHARD A. LESKE[2]
Enrico Fermi Institute and Department of Physics, University of Chicago, Chicago, IL 60637
Received 1992 June 23; accepted 1992 September 16

ABSTRACT

Measurements of the relative elemental and isotopic abundances of iron-group Galactic cosmic rays at energies of ~325 MeV per nucleon have been made using data collected from 1978 to 1981 by the high-energy cosmic ray detector aboard the *ISEE 3* spacecraft. Assuming a standard leaky box model of cosmic-ray propagation, it is found that the source abundance ratio of $^{60}Ni/^{58}Ni$ is 1.07 ± 0.39, which is a factor of 2.8 ± 1.0 larger than the solar system value. Our measurements imply the presence of ^{59}Co at the source, which can be reconciled with the predictions of conventional nucleosynthesis models if there exists a time delay of $\gtrsim 10^5$ yr between nucleosynthesis and acceleration. Most of the ^{54}Mn produced by spallation during cosmic-ray propagation in the Galaxy is found to have decayed to ^{54}Fe, indicating a confinement time of greater than 2 Myr. The source ratio of $^{54}Fe/^{56}Fe$ corrected for the ^{54}Mn decay is 0.046 ± 0.020, which is consistent with the solar system value of 0.063. The source ratio $^{55}Mn/^{56}Fe = 0.025 \pm 0.010$ is a factor of 2.1 ± 0.8 greater than solar. Also, the value of the Cr/Fe elemental ratio is found to be marginally enhanced. The isotope ^{52}Cr appears to be present in the cosmic-ray source at almost the 95% confidence level. The limits obtained on the abundances of the lighter iron-group elements at the source are Sc/Fe < 0.005, Ti/Fe < 0.007, and V/Fe < 0.005.

Subject headings: cosmic rays — ISM: abundances

1. INTRODUCTION

Cosmic-ray nuclei constitute one of the few samples of Galactic matter from outside the solar system that is available for direct analysis. As such, they contain a record of stellar nucleosynthesis processes and Galactic chemical evolution which may be potentially quite different from that found in solar system (SS) material. Prior to arriving at Earth, these particles undergo acceleration and may experience collisions with atoms in the interstellar medium (ISM), resulting in changes in spectra and composition. Detailed studies of cosmic-ray composition, both elemental and isotopic, over a wide range of energies and species are necessary to disentangle the effects of these processes and reveal the composition of the Galactic cosmic-ray source (GCRS).

Iron and nickel have special significance for understanding the origin of cosmic rays. Produced under extreme conditions in the final stages of stellar fusion reactions, ^{56}Fe has the largest binding energy per nucleon of all nuclides, and is generally thought to be synthesized as the unstable progenitor species ^{56}Ni. The mixture of Fe or Ni isotopes produced has been shown to depend sensitively on the neutron excess $\eta = (n_n - n_p)/(n_n + n_p)$, where n_n and n_p are, respectively, the neutron and proton densities (both free and bound in nuclei) of the nucleosynthesis environment. In order to reproduce the observed solar system abundances of these isotopes, particularly the neutron-rich species ^{58}Fe and ^{62}Ni, a mixture of material from at least two regions of very different values of η is required for production under conditions of nuclear statistical equilibrium (Hainebach et al. 1974). More detailed models of explosive nucleosynthesis (Woosley, Arnett, & Clayton 1973; Truran 1992) also require an additional source of ^{58}Fe, such as neutron-capture reactions on ^{56}Fe (Lamb et al. 1977). Measuring the isotopic composition of Fe and Ni in cosmic rays would shed light on how the nucleosynthetic history of these particles differed from that of solar system material. Isotopic anomalies in the form of excess abundances of neutron-rich isotopes of Ne, Mg, and possibly Si have in fact been found in the GCRS (see review by Mewaldt 1989), and the explanations that have been proposed in terms of Galactic chemical evolution (Woosley & Weaver 1981), contributions from unusual stellar sources such as Wolf-Rayet stars (Prantzos et al. 1985), and unique conditions of solar system formation (Olive & Schramm 1982) make some predictions as to what the Fe and Ni isotopic composition should be.

Also of interest in the iron-group region are various radioactive isotopes, the abundances of which provide information about time scales associated with cosmic-ray processes. Above energies of several hundred MeV per nucleon, cosmic-ray nuclei are fully stripped of their orbital electrons and species which decay only by the process of electron capture (ec) are therefore stable. For ec isotopes such as ^{56}Ni, ^{57}Co, and ^{59}Ni whose abundances at the source in the absence of ec decay are expected to be large compared to secondary contributions from the spallation of heavier species en route to Earth, abundance measurements would serve to indicate how much time these particles may have spent at low energies allowing decays to take place before acceleration to higher energies where the nuclei become fully stripped. Knowledge of this time scale would help to distinguish whether cosmic rays are a sample of freshly synthesized supernova ejecta or an accelerated sample of the ISM. A second type of cosmic-ray clock consists of secondary species that are unstable to β decay, such as ^{54}Mn or the lighter species ^{10}Be, ^{26}Al, and ^{36}Cl. The abundances of these isotopes reflect the amount of time spent by the cosmic rays in the ISM after acceleration and before loss from the Galaxy.

Many aspects of the composition of iron-group cosmic rays are incompletely known. Previous studies have established

[1] Submitted to the Department of Physics, University of Chicago, in partial fulfillment of the requirements for the Ph.D. degree.

[2] Postal address: Downs Laboratory of Physics, California Institute of Technology, Pasadena, CA 91125.

that the abundances relative to Fe of the subiron elements such as Sc, Ti, and V are factors of ~1000, ~40, and ~200, respectively, higher in the arriving cosmic rays than their corresponding values in solar system material, due to the production of these species by spallation reactions in collisions between primary cosmic-ray Fe nuclei and interstellar gas atoms. The source contributons to these species are entirely masked by this secondary background.

Determinations have been made of the source abundances of some of the Fe and Ni isotopes. In particular, it has been demonstrated that ^{56}Fe is the dominant Fe isotope at the cosmic-ray source (Mewaldt et al. 1980), as it is in the solar system. The ^{54}Fe/^{56}Fe ratio at the source is consistent with the solar value, with a large uncertainty. Both ^{58}Ni and ^{60}Ni are present in the source (Tarlé, Ahlen, & Cartwright 1979; Young et al. 1981).

Previous attempts to measure the confinement time of iron-group cosmic rays using the ^{54}Mn clock isotope have generally been limited to elemental measurements (Koch et al. 1981) and have proven inconclusive (Grove et al. 1991). Determining the amount of ^{54}Mn decay is important, however, for the proper interpretation of the measured ^{54}Fe abundance, since ^{54}Fe would be produced by the β^- decay of ^{54}Mn (Grove et al. 1991).

No previous isotopically resolved measurements of the Co composition exist, but an attempt has been made by Koch-Miramond (1981) to determine the time delay between the synthesis of iron-group elements and their acceleration to cosmic-ray energies using the Co/Fe elemental abundance ratio to essentially infer the amount of ^{59}Co present (Soutoul, Cassé, & Juliusson 1978). This result has recently been called into question by Webber & Gupta (1990) by using new values for the Co production cross sections (Webber, Kish, & Schrier 1990b, c, d). Actual isotopic measurements would provide important information to help resolve the issue.

We report observations of elemental and isotopic abundances of iron-group cosmic rays made with an instrument on the *ISEE 3* spacecraft. These include new measurements of the Fe isotopes with improved statistics as well as the first satellite-based determination of the isotopic composition of Sc through Mn and Ni. Also, the first reported measurement of the Co isotopic composition is presented. Some of these results have previously appeared in preliminary form (Leske & Wiedenbeck 1990; Wiedenbeck 1990), and the major isotopic results for Mn, Fe, Co, and Ni have been reported by Leske, Milliken, & Wiedenbeck (1992). In this paper we extend the analysis to elements as light as Sc and include discussion of the elemental abundances, as well as present the details of the data analysis and propagation model used to derive the source abundances.

The organization of this paper is as follows. The instrument used for these measurements is briefly described in § 2. The data analysis is discussed in § 3, including descriptions of the various corrections and consistency cuts applied to the data and details of the peak shape model used in fitting the resulting mass distributions. The observed elemental and isotopic composition of the arriving cosmic rays is presented in the tables and figures of § 4. Section 5 gives the details of the propagation model and the inferred source abundances, and includes discussions of our findings for the various species on an element-by-element basis. Our major results are summarized in § 6.

2. INSTRUMENTATION

The instrument used for this analysis (Greiner, Bieser, & Heckman 1978) was designed and constructed by the University of California at Berkeley and flown aboard the *International Sun-Earth Explorer 3* (*ISEE 3*) spacecraft. The data discussed here were collected from 1978 August to 1981 April, during which time the spacecraft was in a so-called halo orbit about the inner Earth-Sun Lagrange point (L1).

A schematic cross section of the instrument is shown in Figure 1. This instrument consists of three pairs of drift chambers (labeled X1, Y1 through X3, Y3) followed by a stack of 10 lithium-drifted, silicon solid-state detectors (D1 through D10) surrounded by a plastic scintillator shell (*S*) which serves as a guard counter to tag particles which enter or exit the side of the stack. Each silicon detector has an active area 44 mm in diameter and is ~4.7 mm thick. Since each chamber is rotated by 90° from the previous one, the drift directions for the X2 and Y2 chambers are oppositely directed from those of the front and back chambers as indicated by arrows in Figure 1. The chambers are not pulse-height analyzed; only timing information is recorded using time-to-digital converters (TDCs), with the start pulse produced by the coincidence of the first two silicon detectors.

For particles which stop in the instrument, corresponding to an energy interval of 200–450 MeV per nucleon for Fe nuclei, a measurement of the energy loss rate ΔE is made in each silicon detector through which the particle passes and the residual energy E' is obtained from the detector in which the particle stops. Using position information from the drift chambers, the trajectory of the particle can be determined and the angle of incidence, θ, between the particle trajectory and the normal to the detector surfaces can be found. This enables the ΔE measurements to be corrected for the path length through the detectors, and allows particle identification (both charge, Z, and mass, M) using the standard dE/dx versus E' technique (see review by Goulding & Harvey 1975).

3. DATA ANALYSIS

3.1. *Event Selection Criteria*

In order for an event to be considered for analysis, it must first satisfy an onboard coincidence between all six drift chambers and the first two silicon detectors, with no signal in the

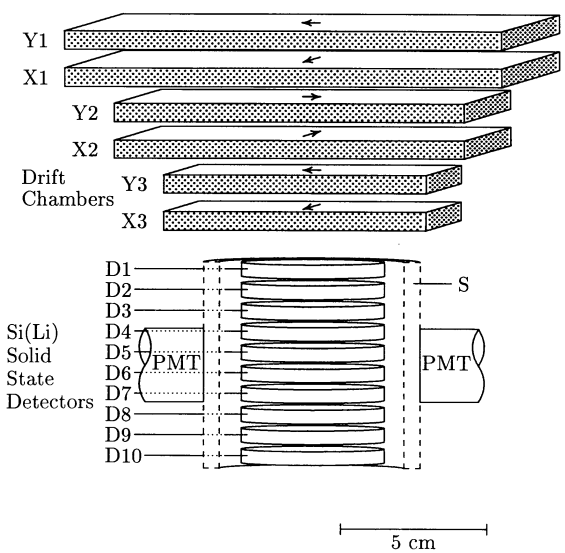

FIG. 1.—Schematic cross section of the *ISEE 3* high-energy cosmic-ray detector. Arrows on the drift chambers indicate the direction of electron drift in each chamber.

guard scintillator or the D10 detector. We impose the further constraint that the particle must stop in D3 or deeper, since at least two ΔE measurements are required to make charge consistency cuts described in § 3.3. Also, we require that none of the six drift chamber times be zero, and that the general pattern of pulse heights in the silicon detector stack be consistent with that of a single-particle event.

3.2. *Trajectory Determination*

Since particles with incidence angles of up to 50° are able to satisfy the above requirements, path lengths through the silicon detectors vary by factors as great as sec 50° = 1.56 and thus determining and correcting for θ is of paramount importance in interpreting the ΔE measurements. No position-dependent mapping corrections to the silicon detector or drift chamber signals are needed due to their known uniformity (Walton et al. 1978; Greiner et al. 1977; Bieser et al. 1977), therefore the absolute positions of individual tracks do not need to be determined, and all that is required is a calculation of θ in terms of the six drift chamber TDC channel numbers. Use of the measurements from the center pair of chambers is complicated, however, by their inverted drift direction along with observed time walk variation with pulse height in the drift chambers. (As an example of this time walk, the mean drift time averaged over all angles of incidence is 5% less for Fe nuclei stopping in D3 than it is for Si nuclei with the same range). Since a difference of two coordinate measurements is required in calculating the angle, any offsets in the drift times will at least partially cancel if the drift directions of both measurements are the same but will add if the drift directions are opposite. Precise determination of the amount of time walk offset on an event by event basis is impossible due to the absence of pulse height information from the drift chambers. We therefore take advantage of the offset cancellation and use only drift time measurements from the outer pairs of chambers to determine θ while incorporating measurements from the center pair to apply a relatively loose trajectory consistency cut.

3.2.1. *Incidence Angle*

Although the drift chambers were tested at a heavy ion accelerator before flight, observed changes in their response, possibly due to differences in the pressure and/or purity of the gas filling between testing and launch, cause us to depend on flight data for their calibration. Since the range of a particle of charge Z and mass M scales from the range of a proton at the same velocity by a factor of M/Z^2, we have

$$L \sec\theta = \frac{M}{Z^2}\left[R_p\left(\frac{\Delta E + E'}{M}\right) - R_p\left(\frac{E'}{M}\right)\right], \qquad (1)$$

where L is the thickness of the silicon detector used for the ΔE measurement and $R_p(E/M)$ is the range-energy relation for protons in silicon (Andersen & Ziegler 1977, modified as described in § 3.3). Therefore if Z and M of the particle were somehow known, θ could be ascertained from the silicon detector signals alone and compared to the set of measurements in the drift chambers to establish a relation between the two. Without a priori knowledge of Z, M, or θ, an iterative approach is required. An initial estimate of Z for each event may be obtained by numerically solving equation (1), using a first approximation of sec θ derived from simple geometrical considerations and an approximation of the nuclear mass M by a piecewise linear function $M(Z)$ through the mean mass for each element. We then select those events due to an element with good statistics and known to be dominated by a single isotope (such as Fe), assign Z and M to the values appropriate for that dominant isotope, and solve equation (1) for sec θ. Assuming linearity between spatial positions in the chambers and the corresponding TDC channel numbers, $\sec^2\theta$ may be expressed as a quadratic function of the TDC channel numbers of the four outer chambers in terms of 11 unknown coefficients. Using the value of $\sec^2\theta$ from equation (1) as the dependent variable, a least-squares fit is performed to solve for these coefficients, treating them as independent parameters. This then provides the desired relation between the TDC channel numbers and sec θ. Iterating the above procedure improves the determination of Z and M and thus allows a more reliable selection of the events to be used in the fit.

In our analysis, this calibration procedure was carried out separately for Fe and Si nuclei, and the coefficients obtained for these two elements were found to differ by ~2%. Some dependence on time, t, was also observed. The coefficients on the terms linear in the position coordinates were found to vary by ~10% over the ~980 day time interval, while those of the quadratic terms were essentially constant. The final formulation for sec θ includes linear corrections in Z and t for the observed variations of the coefficients.

3.2.2. *Trajectory Consistency*

Although positions in the middle pair of drift chambers cannot be measured accurately enough relative to those in the other chambers to improve the precision of the angle determination, they can be used to check that the inferred particle trajectory was reasonably consistent with a single straight line. Apparent inconsistencies may be caused by the passage of a second particle, such as a proton, through a chamber within a few μs of a good event if it produces an inappropriate stop pulse, or by pulse height fluctuations in the start signals and proportional wire signals.

The consistency measure we calculate, x_{con}, is defined as $x_{con} = \frac{1}{2}(x_1 + x_3) - x_2$, where x_i is the measured position in the Xi chamber. Parameterizing this relation in terms of the three TDC channel numbers and four unknown coefficients (including an offset), we solve for the best least-squares fit for the coefficients which minimize x_{con}. As was the case for the angle determinations, corrections to the coefficients which are piecewise linear in t and Z are derived. In addition, a dependence on the D1 pulse height is found, apparently resulting from time walk in the start signal. A similar procedure is used to determine y_{con} from the Y chamber coordinates.

After correction for the t, Z, and D1 pulse-height dependences, the resulting x_{con} and y_{con} distributions are approximately Gaussian in shape, with rms widths of $\sigma_x = 1.74$ mm and $\sigma_y = 1.58$ mm, respectively. About 30% of the events failing a 4 σ cut in both x_{con} and y_{con} are found to be associated with an abnormally low pulse height in D1 and are due to particles which clip the edge of the D1 detector. The short D1 path length and low pulse height results in a late start signal and causes the subsequent trajectory inconsistency.

3.3. *Charge Determination*

Unlike the case of the drift chambers, pre-flight pulser and accelerator calibrations of the silicon detectors and associated electronics have been found to be quite reliable. Only small corrections (no larger than 0.5%) were required to balance relative detector gains using flight data. Also, the response of the detectors was stable throughout the flight.

The charge determination makes use of equation (1), where sec θ is determined from the (now calibrated) drift chambers. For the proton range-energy relation in silicon, we use the expression for dE/dx provided by Andersen & Ziegler (1977), which consists of the Bethe-Bloch formula for the energy loss of charged particles together with an empirically derived term for shell corrections in various media. We find that using this expression (with standard Z^2 scaling) results in a systematic shift in the mass scale for calculations using ever increasing numbers of ΔE detectors. In addition, the absolute mass scale is in error by nearly one mass unit at Fe. By empirically adding small velocity-dependent terms to the expression for dE/dx, and adjusting the value of the effective ionization potential as is commonly done to fit experimental data when deriving range-energy tables (Ziegler 1980), both these problems are reduced. The treatment of residual mass scale errors of ~ 0.2 amu is discussed in § 3.5 below. We scale the adjusted value of dE/dx by $(Z_{\rm eff}/Z)^2$ at each energy, where $Z_{\rm eff}$ is the effective charge of a nucleus accounting for electron attachment at low velocities, using the empirical formulation of Ziegler (1980). Numerical integration of this scaled dE/dx produces a range-energy table which serves as the function $R_p(E/M)$ in equation (1).

When calculating the charge, we use an approximate function for the mass, $M(Z)$, as described in § 3.2.1. We also correct the energy loss ΔE for unmeasured losses, δE, in dead layers, which are assumed to be 10 μm thick for each detector. The charge is calculated iteratively, updating the values of δE and $M(Z)$ with each iteration.

The value of Z we use for the reported elemental abundances is calculated using the energy in the detector in which the particle stops as E' and the energy in the detector immediately preceeding the stop detector as ΔE. We also determine the charge using two other combinations of energy measurements to produce a charge consistency measure, $Z_{\rm con} = 2(Z_{1\Delta E} - Z_{1E'})/Z_{1\Delta E} + Z_{1E'})$, where $Z_{1\Delta E}$ is calculated using the energy deposited in D1 as ΔE with the sum of the energies in D2 through the stop detector as E', and $Z_{1E'}$ is obtained using the energy in the stop detector as E' with the sum of the energies in all previous detectors as ΔE. A plot of $Z_{\rm con}$ versus Z for events which satisfy the selection criteria and trajectory consistency cuts is shown in Figure 2. Events with high ($\gtrsim 1\%$) values of $Z_{\rm con}$ generally have anomalously low values of $Z_{1E'}$ and tend to cluster into diagonal tails extending from the Z-associated concentrations of events near $Z_{\rm con} \sim 0$, most notably from Fe. Analysis of the trajectories for these events and their patterns of pulse heights in the silicon detectors shows that they are due to particles which exited the side of the stack and avoided detection in the anticoincidence guards, some by passing through the gap between D10 and the scintillator and others by stopping in dead material (such as silicon detector mechanical supports) before reaching the scintillator. Similarly, the particles which produce a low value of $Z_{\rm con}(\lesssim -1\%)$ are primarily those which pass through the edge of the D1 detector, yielding an anomalously low value of $Z_{1\Delta E}$ and, as described earlier, poor trajectory consistency as well. In addition to these geometrical reasons for values of $Z_{\rm con}$ to be far from zero, particles which undergo a charge-changing nuclear interaction in the detector will have a poor charge consistency.

We select for further analysis only those events with values of $Z_{\rm con}$ within 4 σ of the mean, as indicated by the dashed lines in Figure 2. The kink above Ni results from adopting the average mean and standard deviation obtained from all higher

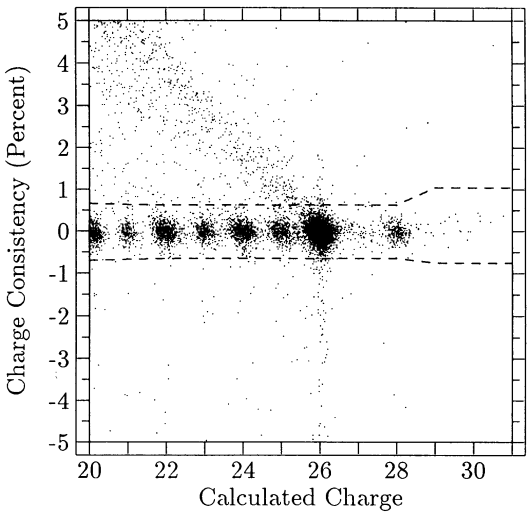

FIG. 2.—Scatter plot of charge consistency (defined as the percent difference between two calculations of the charge as described in the text) vs. charge. The dashed lines indicate the 4 σ limit at which a data cut is made, where the adopted value of σ varies in a piecewise linear manner across the charge range.

Z events to improve the statistics, without accounting for what may be a slight upward bend in the data. Note, however, that even if the trend seen below Ni were extrapolated to the region beyond $Z = 28$, no additional events would be rejected.

To summarize the results of the $Z_{\rm con}$, $x_{\rm con}$, and $y_{\rm con}$ cuts, we find a correlation between the trajectory consistency and charge consistency, largely resulting from the use of D1 in the drift chamber start signal. Most of the background is produced by events that are not fully contained within the stack, and rejection of such events is in no way charge-dependent. Of the 13,112 events (before restricting θ) with $Z \geq 20.5$ satisfying the selection criteria of § 3.1, 69.3% remain after implementing both the charge and trajectory consistency cuts at the 4 σ level.

3.4. *Mass Determination*

The mass resolution of this instrument is dominated by uncertainties in the trajectory determination and improves for smaller values of θ in a manner discussed in § 3.5. Using only events with $\theta \leq 15°$, the charge resolution ($\sigma_Z = 0.072$ charge units at Fe) is such that an unambiguous determination of the charge can be made and an integer value of Z assigned to each event. Equation (1) is then solved for M, correcting for energy losses in dead layers as before.

We calculate M for each remaining event using all possible combinations of energy measurements which involve only one ΔE detector, with the sum of the energies in all detectors beyond the appropriate ΔE detector to the stop detector used as E' in each case. The mean value of the mass obtained was found to vary slightly depending on the combination of detectors used in the calculation and the range of the particle. A set of small correction factors, typically less than 0.2% in size, was empirically determined for each detector combination and used to adjust the position of the mass peaks. The resulting mass values were averaged, with each weighted by a factor reflecting the measured relative resolution arising from the particular combination of energy measurements used in its calculation. By obtaining M in this manner, we not only utilize the maximum amount of information possible from the measurement, but we also can define a χ^2 statistic relating each $1\Delta E$ mass calculation to the average of all such mass calculations

for the event. For all isotopic measurements in this study, we require that the probability of obtaining, by chance alone, a value of χ^2 less than the value calculated for the event be less than 95%. Approximately 18% of the remaining events are eliminated by this cut. The events removed include those located at the bases of the tails in Figure 2 that survived the much looser charge consistency cut, and possibly some due to particles which underwent a neutron-stripping interaction.

3.5. *Maximum Likelihood Parameter and Abundance Fits*

The mass resolution obtained for iron-group species from this instrument is ~0.60 amu, even after restricting θ to less than 15°. While sufficient for studying the relative abundances of isotope pairs such as ^{57}Co and ^{59}Co with a 2 amu separation and little or no abundance of the intervening isotope, in general this resolution results in considerable overlap between adjacent peaks. To determine the relative abundance of each isotope, maximum likelihood fits of the measured mass distributions were performed. A necessary prerequisite for this procedure is a model of the peak shape for each isotope. We find that each mass peak is well represented by a superposition of Gaussians of unit area, one for each event in the peak, where the mean and standard deviation of each Gaussian depend on the values of Z and θ of the event. This dependence may be parameterized and the best values of these parameters over a wide range of Z ($14 \lesssim Z \leq 28$) and θ ($0° \leq \theta \leq 30°$) are obtained from the maximum likelihood fits.

The calculated position of the mass peak was observed to decrease slightly at larger values of θ (by ~0.4% between $\theta = 0°$ and $\theta = 15°$) and was empirically corrected. The resulting mass values differ by up to ~0.2 amu from the expected integer values, with the amount of the deviation depending on Z as shown in Figure 3. These deviations are fit reasonably well by a parabola for $14 \leq Z \leq 28$, as shown by the solid curve in the figure, and appropriate shifts to the mass scale are applied. In addition to such shifts of the entire mass distribution of a particular element, we also considered the possibility that the peak-to-peak spacing between the isotopes within a distribution may differ from the nominal 1 amu. By allowing this spacing to be a free parameter and using all

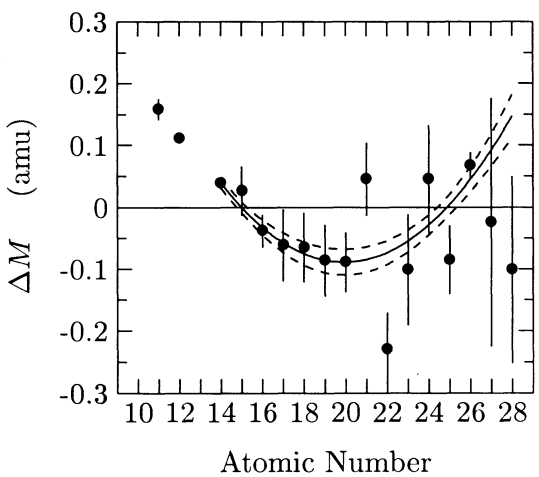

FIG. 3.—Deviation from integer values of the mean position of the dominant mass peak for each element, obtained by allowing the mass position to be a free parameter in a maximum likelihood fit of the abundances. The best parabolic fit to the region from Si to Ni is also shown (*solid curve*), along with the 1 σ error limits (*dashed curves*).

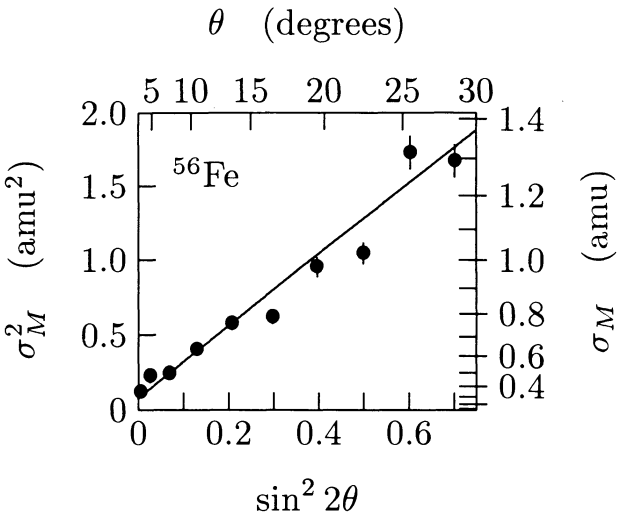

FIG. 4.—Variation of the mass resolution σ_M with incidence angle θ, illustrating the linear relationship between σ_M^2 and $\sin^2 2\theta$. For reference, the corresponding value of θ is shown across the top abscissa, and along the right ordinate the value of σ_M is displayed. The data points represent measurements of the width of the ^{56}Fe peak using 3° wide angle bins. The solid line is obtained from parameters derived to fit all data from $Z = 14$ to 28 with $\theta < 30°$ and is not specifically fit to the iron data shown here.

multi-isotope elements from Si to Ni, we find that this value is consistent with 1 amu (0.995 ± 0.015), with no discernible Z dependence.

As noted previously, the mass resolution depends strongly on the incidence angle θ. A straightforward calculation shows that $\sigma_M(\theta)$, the contribution to the mass resolution due to trajectory measurement errors, may be expressed as

$$\sigma_M^2(\theta) = \left(\frac{\partial M}{\partial \sec\theta}\right)^2 (\delta \sec\theta)^2 = \frac{\delta x_1^2 + \delta x_3^2}{4(\alpha - 1)^2 \Delta z^2} M^2 \sin^2 2\theta , \quad (2)$$

where δx_i is the uncertainty on the measured position in the Xi drift chamber and Δz is the center-to-center spacing between the X1 and X3 (or Y1 and Y3) chambers. This assumes that $\delta x_1 \simeq \delta y_1$, $\delta x_3 \simeq \delta y_3$, and that the proton range is written as a power law in energy per nucleon with index α. We therefore write $\sigma_M^2 = A^2 + B^2 M^2 \sin^2 2\theta$, where A includes all contributions to the resolution other than those due to angle uncertainties and B is a constant. From the maximum likelihood fits, we find that the value of A increases linearly with Z, while B is constant, with a value of $(2.77 \pm 0.08) \times 10^{-2}$. Using the known values for Δz and α, and assuming $\delta x_1 \simeq \delta x_3$, we obtain from equation (2) a position uncertainty of ~1.25 mm, which is reasonably consistent with the known performance of the drift chambers (Bieser et al. 1977). The agreement between the model and the data is further illustrated in Figure 4, a plot of σ_M^2 versus $\sin^2 2\theta$ derived from measurements of the width of the ^{56}Fe peak. Thus this simple model provides a good qualitative and quantitative description of the angle dependence of the mass resolution.

With the peak-shape parameters determined and fixed, the maximum-likelihood fit calculations are repeated, solving only for the relative isotopic abundances. The resulting errors on these abundances represent a combination of both statistical and fitting uncertainties. For dominant or well-separated peaks, the errors are primarily statistical, while for low abundance, unresolved species between higher abundance peaks, fitting uncertainties (due to the changing contribution to the

region of the small peak resulting from minor adjustments in the abundances of the neighboring larger peaks) dominate the uncertainties.

Once the mass abundances have been found using the nominal set of peak-shape parameters, these parameters are varied within their allowed 1 σ limits and the abundances recalculated. Each parameter is varied independently, with the resulting uncertainties on the abundances added in quadrature. In general, these systematic errors are smaller by factors of 5 to 10 than the combined statistical and fitting uncertainties. The exception is Fe, where the two types of uncertainties are comparable in size due to the good statistics.

3.6. *Range-to-Energy and Interaction Corrections*

In the instrument used for this investigation, the relative abundance measurements are made over a common range interval for all species. The ratio of the flux of species Z, M to that of a reference species with charge $Z_{\rm ref}$ and mass $M_{\rm ref}$ is converted to that expected if the measurements had been made over equal energy per nucleon intervals by an energy-interval correction factor $f_E = (Z_{\rm ref}^2 M/Z^2 M_{\rm ref})^{(\beta+1)/\alpha}$. Here it is assumed that the spectral shapes are the same for both species, at least over the energy interval of interest, that the proton range-energy relationship may be expressed as a power law with index α, and that the cosmic-ray flux exhibits a power-law spectrum in energy per nucleon with index β. From the modified Andersen & Ziegler (1977) range-energy relation we find $\alpha = 1.63 \pm 0.05$ over the energy and charge interval relevant here, and we take $\beta = 0.0 \pm 0.2$ (Simpson 1983; Tang 1990). The resulting value of f_E ranges from 0.95 for Ni/Fe to 1.14 for Sc/Fe for elemental ratios and from 0.95 for ^{44}Ti/^{48}Ti to 1.04 for ^{62}Ni/^{58}Ni for isotopic ratios of the species under consideration.

An additional small correction factor is applied to the derived abundance ratios to account for the relative differences in the nuclear interaction losses in the instrument for the various species, using the mass-changing total cross section formula of Westfall et al. (1979). For isotopic ratios reported here, this factor differs from unity by less than 1%, ranging from 0.991 for ^{44}Ti/^{48}Ti to 1.008 for ^{62}Ni/^{58}Ni. The correction factor for elemental ratios, assuming a mean mass for each element, has a somewhat greater range, varying from 0.977 for Sc/Fe to 1.007 for Ni/Fe.

4. OBSERVED COMPOSITION

For the elemental analysis, we employ a 4 σ charge consistency cut and 2.5 σ trajectory consistency ($x_{\rm con}$ and $y_{\rm con}$) cuts, and we restrict the incidence angle to $\theta < 30°$. This gives a charge resolution of 0.10 charge units at iron, and results in the charge histogram shown in the upper panel of Figure 5. Several of the peaks, such as those for Ti, Cr, Mn, and Ni, appear rather broad and non-Gaussian in shape due to the presence of several isotopes. Notice also that a small peak is present at $Z \simeq 30$ (Zn). Of the three events with $28.5 \leq Z \leq 29.5$, additional checks, such as the χ^2 test of mass consistency described in § 3.4, suggest that only one may be due to Cu, with the rest more likely a tail on the Ni distribution.

In our earlier paper reporting results for Mn through Ni (Leske et al. 1992), we used a looser trajectory consistency cut of 4 σ. While the charge abundances for the subiron elements are found to change by only $\sim$0.2 standard deviations when the 4 σ cut is tightened to the 2.5 σ level, our older elemental ratios for Co and Ni are about one standard deviation higher than those reported here. We wish to emphasize, however, that the abundance ratios for isotopes within any particular element which we previously reported are completely unaffected by making this cut more restrictive as none of the additional Co or Ni events rejected satisfy the incidence angle requirements for inclusion in the mass analysis. The elemental abundance ratios are found to remain essentially unchanged if the cut is further tightened to the 1.5 σ level.

Table 1 lists the number of events for each element on which the abundance determinations are based, and the derived relative charge abundances at $\sim$325 MeV per nucleon at 1 AU,

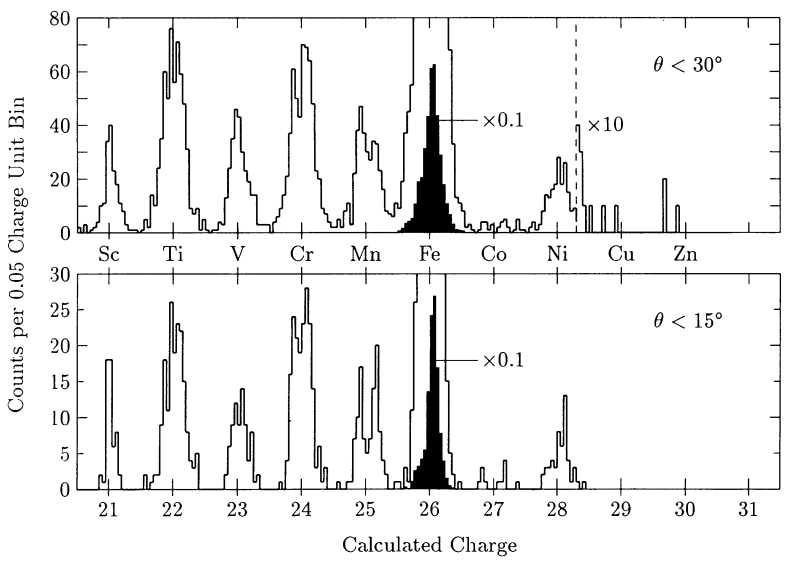

FIG. 5.—Measured charge histograms, with data cuts corresponding to those used for charge analysis (*top panel*) and mass analysis (*bottom panel*). Both sets include a cut on $Z_{\rm con}$ at the ± 4 σ level. The top set uses 2.5 σ trajectory consistency cuts with $\theta < 30°$, while the bottom set employs 4 σ trajectory consistency cuts with $\theta < 15°$ and an additional χ^2 cut at the 95% probability level. Most of the differences in resolution and statistics between the two cases are due to the different θ cuts. Note the scale change above $Z = 28.3$ in the upper panel. The shape of the Fe peak is shown at a reduced scale in each panel. For Fe, $\sigma_Z = 0.10$ charge units in the upper panel, and 0.072 charge units in the lower panel.

TABLE 1

NUMBER OF ANALYZED EVENTS

	Events									
Analysis	Sc	Ti	V	Cr	Mn	Fe	Co	Ni	Cu	Zn
Elemental[a]	168	574	282	563	351	3831	33	194	1	3
Isotopic[b]	55	170	76	186	102	582	12	52	...	...

[a] Z_{con} cut at $\pm 4\,\sigma$ level; x_{con} and y_{con} cut at $\pm 2.5\,\sigma$ level; $\theta < 30°$.
[b] Z_{con} cut at $\pm 4\,\sigma$ level; x_{con} and y_{con} cut at $\pm 4\,\sigma$ level; χ^2 probability cut at 95%; $\theta < 15°$, except for Fe, where $\theta < 10°$ (1128 Fe events for $\theta < 15°$).

after applying the corrections of § 3.6, are listed in Table 2. We compare our measurements with those made by other investigators in Figure 6, where we also show, as a function of energy, charge ratios expected if the cosmic-ray source abundances are the same as those in the solar system, based on a propagation model described in § 5.1. Some of these curves, such as that for Mn, do not provide a good fit to the data, which suggests that the source abundances may be nonsolar. For Cu and Zn, we indicate the actual solar values instead of the propagated values, since our propagation program is not equipped to treat species with $Z > 28$. Since the destruction cross sections of Zn, Cu, and Fe are similar, and since secondary contributions to Cu and particularly Zn should be negligible, the results of a proper propagation calculation would not be expected to differ greatly from the solar value in any case. Our results are generally in good agreement with other measurements, particularly the *Voyager 2* results (allowing for the differences in solar modulation, as shown by Ferrando et al. 1991) and the lower energy *HEAO 3* C2 data. Our Co/Fe value is a factor of ~ 1.7 (or 2.8 σ) higher than the *HEAO* result. The value obtained is consistent with that found using more restrictive cuts (Fig. 5, bottom panel), and therefore this excess does not appear to represent inadvertent identification of Fe or Ni events as Co. Our Zn/Fe measurement represents the first satellite-based determination of this ratio at low energies. While we cannot rule out the solar value due to the large statistical errors, this measurement agrees with the other higher energy results and may support the finding that the cosmic-ray Zn/Fe source ratio is substantially lower than the corresponding solar system value (Tueller et al. 1979; Binns et al. 1981; Byrnak et al. 1983). This depletion appears to be due to the well-known correlation between elemental abundance and first ionization potential (FIP), since Zn has a FIP value of 9.39 eV which is above the break at ~ 8.5 eV (see review by Lund 1989). We note that the other abundances considered here are not expected to be affected by such fractionation, since the FIP values for the elements involved range from 6.54 eV (Sc) to 7.87 eV (Fe).

TABLE 2

COSMIC-RAY RELATIVE ELEMENTAL ABUNDANCES AT 325 MeV PER NUCLEON NEAR EARTH (Fe = 100)

Element	Measured Value	Propagated Solar[a]
Sc	4.87 (+0.44, −0.37)	4.69
Ti	16.30 (+0.84, −0.77)	16.37
V	7.87 (+0.53, −0.47)	7.54
Cr	15.27 (+0.74, −0.67)	14.07
Mn	9.38 (+0.56, −0.50)	8.08
Co	0.85 (+0.18, −0.13)	0.59
Ni	4.82 (+0.39, −0.33)	4.85
Cu	<0.083	0.058[b]
Zn	0.074 (+0.072, −0.022)	0.14[b]

[a] Grevesse & Anders 1989; Anders & Ebihara 1982 source composition, assuming β^- decay of ^{54}Mn with $\tau_{esc}/T_{\beta^-} = 110$.
[b] Solar value without propagation.

For the mass analysis, the charge and trajectory consistency cuts are made at the 4 σ level and the χ^2 requirement described in § 3.4 is cut at the 95% probability level. We restrict the incidence angle to less than 15° for all elements except Fe, where we use $\theta < 10°$ to improve the resolution. A charge histogram of the remaining events (using $\theta < 15°$ throughout) is shown in the lower panel of Figure 5. Note the clean separation of the charge peaks, as well as pronounced structure in the peaks due to individual isotopes. The mass distributions obtained from this data set are shown in Figure 7, with the total numbers of events appearing in each distribution listed in Table 1. Superposed on the histograms are curves showing the best fits derived for each isotope and the overall fitted distribution obtained using the maximum likelihood technique and peak-shape model discussed in § 3.5. Due to the sensitivity of the fitting technique to outlying events in tails, only events in the region within ± 1 amu of the mass of a stable or long-lived isotope were used in determining the goodness of fit. This restriction has a significant effect only on Co, where two of the total 12 events fall below mass 56.0. The nature of these events is unclear. Spillover from Fe would be expected to produce a smooth tail on the Fe distribution, which is not seen (Fig. 5, *bottom*). Also, if these events were due to Fe particles, their calculated mass would be $\gtrsim 60$, which is highly unlikely. The uncertainty in the identification of these events is reflected in a corresponding increase in the error we quote for the measured ^{59}Co/^{57}Co abundance ratio. Note that the fits shown are only the best values obtained from the fitting procedure and give no indication of the uncertainties, which can be considerable for poorly separated isotopes. In Table 3 we list our measured values of the isotopic fractions and in Table 4 the isotopic ratios for each element, including the uncertainties, and compare our measurements with the values expected for a propagated solar source composition. For some species, particularly ^{55}Fe, ^{57}Fe, and ^{58}Fe, while our best-fit values differ from zero by more than 2 σ, the isotopes are not resolved into distinct peaks and the accuracy of the abundance determinations therefore depends strongly on the reliability of the peak-shape model. Since we cannot be completely certain that this model accurately represents any far tails of the ^{56}Fe distribution, we conservatively treat these measurements as upper limits. Our measured mass fractions are compared with those obtained by other investigators in Figure 8, and are found to be generally similar to those expected for a solar source composition. The derived source abundances with their uncertainties are presented in § 5.2, along with a discussion of the deviations from solar abundances.

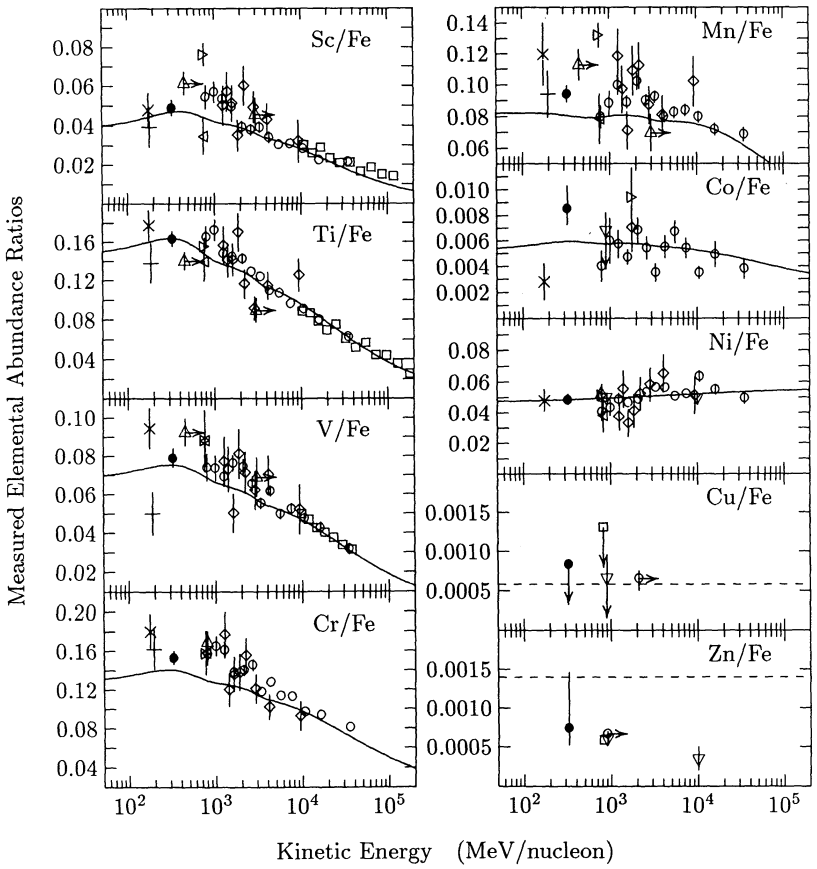

FIG. 6.—Measured elemental abundance ratios as a function of energy per nucleon. Solid curves are propagation results assuming the cosmic-ray source composition is solar and that $\tau_{esc}/T_{\beta}(^{54}\mathrm{Mn}) = 110$, with a solar modulation parameter of $\phi = 740$ MV. Dashed lines for the Cu/Fe and Zn/Fe plots indicate actual solar values without propagation. Horizontal errors are suppressed for clarity, and vertical error bars are omitted when smaller than the plotted symbol. Data points shown with arrows to the right indicate values reported as integral measurements above the energy at which the point is shown. References for the data and instruments used for the measurements are the following: (*filled circle*) this work, *ISEE 3*; (+) Ferrando et al. (1991), *Voyager 2*; (×) Garcia-Munoz & Simpson (1979), *IMP 8*; (*triangle with point right*) Young et al. (1981), balloon; (*triangle with point left*) Henkel et al. (1990), balloon; (*diamond*) Dwyer & Meyer (1987), balloon; (*open circle*) Engelmann et al. (1990) and Byrnak et al. (1983), *HEAO 3* C2; (*square*) Vylet et al. (1990) and Binns et al. (1981), *HEAO 3* C3; (*triangle with point up*) Webber (1982) and Lezniak & Webber (1978), balloon; (*triangle with point down*) Tueller et al. (1979), balloon.

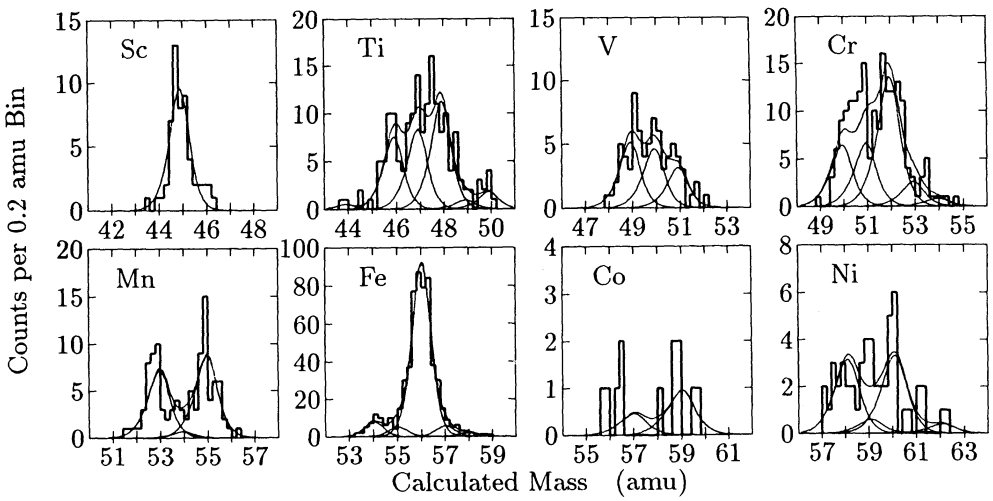

FIG. 7.—Measured mass histograms for the elements Sc through Ni. Smooth curves show the maximum likelihood fits used to obtain relative isotopic abundances. Events more than one mass unit away from the mass of a stable or long-lived isotope are not included in the fits, as discussed in the text.

TABLE 3

COSMIC RAY ISOTOPIC COMPOSITION AT 325 MeV PER NUCLEON NEAR EARTH: MASS FRACTIONS

Ratio	Measured Value	Propagated Solar[a]
^{44}Ti/Ti	0.015 (+0.013, −0.008)	0.0087
^{46}Ti/Ti	0.240 (+0.040, −0.039)	0.272
^{47}Ti/Ti	0.273 (+0.054, −0.057)	0.304
^{48}Ti/Ti	0.376 (+0.061, −0.054)	0.330
^{49}Ti/Ti	<0.066[b]	0.073
^{50}Ti/Ti	0.063 (+0.026, −0.021)	0.0116
^{49}V/V	0.391 (+0.074, −0.073)	0.509
^{50}V/V	0.359 (+0.092, −0.088)	0.337
^{51}V/V	0.250 (+0.073, −0.066)	0.155
^{50}Cr/Cr	0.206 (+0.053, −0.042)	0.165
^{51}Cr/Cr	0.218 (+0.057, −0.056)	0.259
^{52}Cr/Cr	0.458 (+0.055, −0.055)	0.457
^{53}Cr/Cr	0.089 (+0.040, −0.036)	0.085
^{54}Cr/Cr	<0.052[b]	0.030
^{53}Mn/Mn	0.421 (+0.057, −0.057)	0.458
^{54}Mn/Mn	<0.095	0.058
^{55}Mn/Mn	0.538 (+0.058, −0.059)	0.484
^{54}Fe/Fe	0.069 (+0.013, −0.012)	0.087
^{55}Fe/Fe	<0.063[b]	0.036
^{56}Fe/Fe	0.815 (+0.024, −0.025)	0.852
^{57}Fe/Fe	<0.071[b]	0.022
^{58}Fe/Fe	<0.029[b]	0.0038
^{57}Co/Co	0.32 (+0.25, −0.14)	0.52
^{59}Co/Co	0.68 (+0.14, −0.26)	0.48
^{58}Ni/Ni	0.408 (+0.095, −0.092)	0.654
^{59}Ni/Ni	<0.20	0.019
^{60}Ni/Ni	0.447 (+0.118, −0.115)	0.260
^{61}Ni/Ni	<0.073	0.017
^{62}Ni/Ni	<0.10[b]	0.037

[a] Calculation assumes β^- decay of ^{54}Mn with $\tau_{esc}/T_{\beta^-} = 110$, solar elemental (Grevesse & Anders 1989) and isotopic (Anders & Ebihara 1982) source composition.

[b] Finite measurement was converted to upper limit.

TABLE 4

COSMIC RAY ISOTOPIC COMPOSITION AT 325 MeV PER NUCLEON NEAR EARTH: MASS RATIOS

Ratio	Measured Value	Propagated Solar[a]
^{44}Ti/^{48}Ti	0.041 (+0.036, −0.023)	0.026
^{46}Ti/^{48}Ti	0.64 (+0.17, −0.16)	0.82
^{47}Ti/^{48}Ti	0.73 (+0.26, −0.23)	0.92
^{49}Ti/^{48}Ti	<0.19[b]	0.22
^{50}Ti/^{48}Ti	0.168 (+0.076, −0.059)	0.035
^{49}V/^{50}V	1.09 (+0.48, −0.34)	1.51
^{51}V/^{50}V	0.70 (+0.42, −0.27)	0.46
^{50}Cr/^{52}Cr	0.45 (+0.14, −0.11)	0.36
^{51}Cr/^{52}Cr	0.48 (+0.18, −0.15)	0.57
^{53}Cr/^{52}Cr	0.194 (+0.108, −0.084)	0.186
^{54}Cr/^{52}Cr	<0.12[b]	0.066
^{54}Mn/^{53}Mn	<0.25	0.126
^{55}Mn/^{53}Mn	1.28 (+0.32, −0.25)	1.06
^{54}Fe/^{56}Fe	0.084 (+0.017, −0.015)	0.102
^{55}Fe/^{56}Fe	<0.078[b]	0.042
^{57}Fe/^{56}Fe	<0.089[b]	0.026
^{58}Fe/^{56}Fe	<0.036[b]	0.0045
^{59}Co/^{57}Co	2.2 (+2.4, −1.4)	0.93
^{59}Ni/^{58}Ni	<0.58	0.029
^{60}Ni/^{58}Ni	1.10 (+0.50, −0.35)	0.398
^{61}Ni/^{58}Ni	<0.19	0.026
^{62}Ni/^{58}Ni	<0.28[b]	0.056

[a] Calculation assumes β^- decay of ^{54}Mn with $\tau_{esc}/T_{\beta^-} = 110$, solar elemental (Grevesse & Anders 1989) and isotopic (Anders & Ebihara 1982) source composition.

[b] Finite measurement was converted to upper limit.

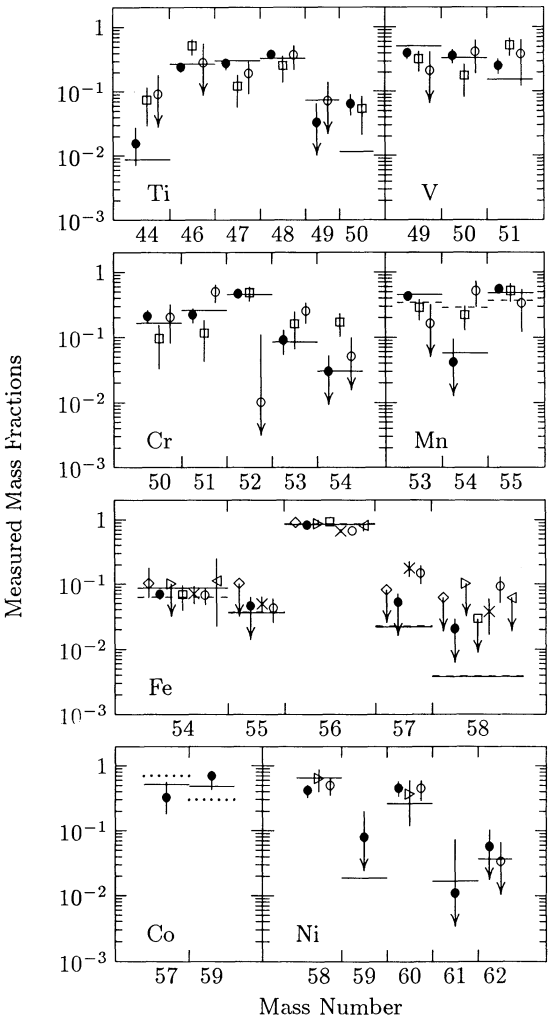

FIG. 8.—Mass fractions measured in the arriving iron-group cosmic rays as obtained in this work compared with those previously determined by other investigators. Solid horizontal lines indicate the values expected from a propagation model assuming a solar source composition and a value of $\tau_{esc}/T_{\beta^-}(^{54}\text{Mn}) = 110$, consistent with the value obtained in this work. For Mn and Fe, dashed lines indicate the mass fractions expected from the model assuming ^{54}Mn is stable to β decay. The dotted lines for Co show the mass fractions expected if Co is purely secondary (Webber & Gupta 1990). Data points are arranged in order of increasing measurement energy. References for the data are the following: (*filled circle*) this work; (*square*) Webber (1981); (*open circle*) Young et al. (1981); (*diamond*) Mewaldt et al. (1980); (*triangle with point right*) Tarlé et al. (1979); (×) Hesse et al. (1991); (*triangle with point left*) Grove et al. (1990). Errors shown on the Hesse et al. (1991) points are estimates of the statistical uncertainties only.

5. INTERPRETATION AND DISCUSSION

5.1. *Propagation Model*

In order to understand the source composition of the observed cosmic rays and interpret the compositional changes that take place during transport, we performed numerical calculations of the effects of propagation using a standard leaky box model, based on the formalism of Meneguzzi, Audouze, & Reeves (1971). In this model, it is assumed that cosmic rays are accelerated to high energies at their source and undergo no further acceleration during their subsequent travel through the Galaxy. During transport, fluxes are subject to modification due to escape of particles from the Galaxy, radioactive decay

(in the case of unstable species) from one species into another, and interactions with the ISM, including both energy loss to ionization of the interstellar matter and nuclear alterations in spallation reactions. The secondary nucleus resulting from a spallation reaction is assumed to have the same energy per nucleon (or velocity) as the primary nucleus from which it was produced.

The number density of hydrogen in the ISM is taken to be 0.3 atoms cm^{-3}, however this value is only important for radioactive species and their daughters since the density (as opposed to total grammage) only appears in terms involving radioactive decay. Following Soutoul, Ferrando, & Webber (1990), we adopt the value of 16% for the ionized fraction of hydrogen in the ISM, which results in an increase of the energy loss in the overall hydrogen component by a factor of 1.4 over the losses in neutral hydrogen alone. We also include the effects of energy losses in helium, and assume the ISM is 10% helium by number (Meyer 1989).

We assume all species have identical source spectra, which we take to be power laws in momentum per nucleon (as in Ferrando et al. 1991) with an index of -2.3 (as in Grove et al. 1991). For the escape mean free path, Λ_{esc}, we use a form derived from the *HEAO 3* C2 measurements (Engelmann et al. 1990), with parameters adjusted to accurately reproduce our Sc + Ti + V/Fe ratio. The resulting expression is

$$\Lambda_{esc} = \begin{cases} 15.6\beta \text{ g cm}^{-2} & \text{for } R \leq 4.9 \text{ GV} \\ 47.5\beta R^{-0.70} \text{ g cm}^{-2} & \text{for } R > 4.9 \text{ GV}, \end{cases} \quad (3)$$

where β is the velocity divided by the speed of light and R is the rigidity in GV. This path-length distribution was found to provide a good fit to all our subiron secondaries at 325 MeV per nucleon as well as to the *HEAO 3* C2 measurements at energies $\gtrsim 5$ GeV per nucleon, however it generally underestimates the *HEAO* values in the energy range of ~ 1 to 5 GeV per nucleon. To test the sensitivity of the resulting source abundances to the choice of Λ_{esc}, we repeated the calculations with a Λ_{esc} empirically adjusted to fit the 1–5 GeV per nucleon measurements as well. The effect on the derived source abundances was small compared to statistical errors (typically ~ 0.1 σ), as is expected since measured elemental ratios at one energy are relatively insensitive to the grammage encountered at much higher energies.

Since most of the observed nuclei between $Z = 21$ and $Z = 25$ are products of spallation reactions, the nuclear interaction cross sections are vitally important for interpreting the abundances of these species. For this analysis, we use the formula based on recent measurements of Webber et al. (1990a) for the asymptotic values of the total charge and mass-changing cross sections in hydrogen and helium, together with the energy dependence formulated by Letaw, Silberberg, & Tsao (1983). For the partial fragmentation cross sections in hydrogen, we use the formulae of Webber et al. (1990b, c, d) and Webber (1991) and scale the resulting values to agree with the cross sections measured by these authors at 600 MeV per nucleon for those reactions where measurements are available. Cross sections in helium are scaled from those in hydrogen using the formulae of Ferrando et al. (1988) and Webber (1991). Spallations to short-lived species unstable to β decay are also treated; such species are assumed to instantly decay to their stable, long-lived, or ec daughter species, with appropriate branching ratios taken from Lederer & Shirley (1978). Values of the "decayed" partial cross sections (applicable after the short-lived β decays have taken place) obtained from the computer code supplied by Webber (1991) or replaced by their measured values are listed in Table 5.

While generally a small effect except at the very lowest energies, if an ec nucleus does attach an atomic electron from the ISM, decay will be likely to occur for species with a mean ec decay time short compared to the electron stripping time of $\sim 10^4$ yr (Wilson 1978). Our calculations therefore include the production and loss of both fully stripped atoms and those with one electron attached for each species. The formulae for the electron stripping and attachment cross sections are taken primarily from Crawford (1979), with the expression for the radiative attachment cross section corrected as in Wilson (1978) and Pratt, Ron, & Tseng (1973).

Before being detected at 1 AU, the cosmic-ray particles must enter the heliosphere, where they encounter the outward flowing solar wind and magnetic fields and experience rigidity-dependent deceleration. In our calculations, the effect of this solar modulation on the interstellar particle fluxes is taken into account by using the approach of Fisk (1971) to solve the spherically symmetric Fokker-Planck equation which includes treatment of the processes of diffusion, convection, and adiabatic deceleration under steady-state conditions. The diffusion coefficient which we use is taken to be directly proportional to the product of the particle velocity and rigidity, and independent of position within the heliosphere. The level of solar activity increased considerably during the interval of our measurements. Using the results of Garcia-Munoz et al. (1987), we estimate that the average level of solar modulation appropriate for the time period of our data corresponds to an average energy loss of $\Phi = 370$ MeV per nucleon for particles with $M/Z = 2$. We allow for a $\pm 20\%$ uncertainty on this value to account for the changing level of modulation during our observations, and find that the error introduced by this uncertainty on the derived source abundances is typically much smaller (~ 0.1 σ) than the statistical errors.

5.2. *Source Abundances*

To derive source isotopic abundances from measurements of the arriving cosmic rays, the propagation calculations must somehow be inverted. This is most easily done by forward propagating a collection of individual sources, each consisting of a single stable or long-lived isotope from ^{64}Ni to ^{45}Sc, to construct a matrix which may be inverted. The source abundances obtained are listed in Table 6, with errors due to uncertainties on the measurements combined with those associated with the uncertainty in the level of solar modulation. Our derived source values for the Fe and Ni isotopic ratios are shown in Figure 9, where they are compared with those obtained by other investigators, with the solar values, and with the values predicted by two models proposed to explain the anomalous isotopic composition of cosmic-ray Ne, Mg, and Si.

To calculate source elemental abundances, an elemental propagation matrix is generated from the isotopic matrix by adding the contributions from all isotopes of an element using a weighted average based on either derived source isotopic abundances or solar system values. The resulting abundances, with errors reflecting uncertainties in the measurements and in the source isotopic composition, are included in Table 6 and compared with those found by others in Figure 10.

5.2.1. *Nickel*

From Table 6, we find that the elemental ratio Ni/Fe at the cosmic-ray source is essentially the same as that in the solar system. This similarity extends to the isotopic composition in

TABLE 5

DECAYED CROSS SECTIONS ON HYDROGEN AT 600 MeV PER NUCLEON, IN MILLIBARNS

	PARENT													
DAUGHTER	^{62}Ni	^{61}Ni	^{60}Ni	^{59}Ni	^{58}Ni	^{59}Co	^{57}Co	^{58}Fe	^{57}Fe	^{56}Fe	^{55}Fe	^{54}Fe	^{55}Mn	^{54}Mn
^{61}Ni	210.2	0	0	0	0	0	0	0	0	0	0	0	0	0
^{60}Ni	41.3	179.4	0	0	0	0	0	0	0	0	0	0	0	0
^{59}Ni	4.3	23.3	102.4	0	0	0	0	0	0	0	0	0	0	0
^{58}Ni	0.0	3.6	19.4	74.2	0	0	0	0	0	0	0	0	0	0
^{59}Co	60.0	31.9	50.0	0	0	0	0	0	0	0	0	0	0	0
^{57}Co	25.1	37.1	53.1	72.3	119.1	14.0	0	0	0	0	0	0	0	0
^{58}Fe	89.9	88.3	56.4	55.0	0	122.2	0	0	0	0	0	0	0	0
^{57}Fe	41.6	54.7	54.3	15.1	0	61.7	0	115.7	0	0	0	0	0	0
^{56}Fe	28.2	51.6	81.3	83.3	76.6	46.6	103.1	28.5	107.0	0	0	0	0	0
^{55}Fe	4.1	13.1	32.6	49.8	66.4	13.3	62.9	4.6	16.4	59.3	0	0	0	0
^{54}Fe	0.3	1.7	6.8	16.1	22.3	1.7	18.8	0.2	3.9	12.2	44.5	0	0	0
^{55}Mn	17.4	13.2	9.7	5.3	2.7	17.4	14.4	29.9	22.1	35.3	0	0	0	0
^{54}Mn	25.0	26.2	25.5	18.2	12.0	31.6	22.3	33.7	37.9	42.3	38.9	0	78.8	0
^{53}Mn	18.7	25.2	31.8	30.9	26.4	27.7	35.7	19.6	29.5	42.2	55.6	74.3	18.7	62.4
^{54}Cr	11.1	6.1	2.7	0.8	0.2	7.4	0.9	16.3	9.1	3.0	0	0	34.8	0
^{53}Cr	24.2	20.2	13.5	6.0	2.1	23.6	7.1	32.4	27.9	11.5	13.6	0	33.0	38.7
^{52}Cr	30.7	41.0	47.8	40.9	33.2	45.2	46.2	35.8	49.4	55.0	54.2	72.4	48.7	64.4
^{51}Cr	10.7	21.1	33.9	37.2	33.3	22.6	41.6	11.3	23.9	41.1	46.2	42.4	24.9	43.8
^{50}Cr	1.9	5.6	13.4	21.4	26.5	5.8	23.6	1.8	6.0	24.1	25.9	33.2	6.0	16.1
^{51}V	7.6	5.6	4.0	2.3	1.1	7.2	2.9	13.1	9.7	6.8	3.8	1.8	13.6	9.4
^{50}V	16.8	16.2	14.7	10.8	6.8	19.6	13.1	24.0	24.1	25.1	16.2	9.9	29.6	27.8
^{49}V	16.9	21.3	26.1	28.0	28.7	24.0	32.2	20.1	26.8	37.3	37.1	37.8	28.9	38.3
^{50}Ti	3.4	1.7	0.7	0.2	0.1	2.1	0.3	5.4	2.6	1.2	0.3	0.1	3.4	1.4
^{49}Ti	12.5	8.9	5.4	2.5	0.9	10.8	3.0	18.1	13.2	7.0	3.7	1.3	16.3	9.9
^{48}Ti	26.4	31.1	33.9	31.2	25.3	35.3	35.8	33.0	39.7	42.0	40.9	33.5	44.2	49.2
^{47}Ti	15.8	22.7	29.7	31.6	26.9	25.8	36.3	20.4	29.2	36.9	41.6	35.6	33.2	43.9
^{46}Ti	12.3	15.4	20.8	26.0	26.0	18.0	30.1	17.7	21.4	31.6	35.0	35.1	25.8	33.2
^{44}Ti	0.0	0.1	0.3	1.0	2.2	0.1	1.1	0.0	0.1	0.7	1.2	2.8	0.1	0.4
^{45}Sc	16.3	17.4	19.4	22.1	22.0	20.6	26.1	22.7	24.4	28.8	30.9	30.4	28.9	32.4

TABLE 5—*Continued*

	PARENT													
DAUGHTER	^{53}Mn	^{54}Cr	^{53}Cr	^{52}Cr	^{51}Cr	^{50}Cr	^{51}V	^{50}V	^{49}V	^{50}Ti	^{49}Ti	^{48}Ti	^{47}Ti	^{46}Ti
^{61}Ni	0	0	0	0	0	0	0	0	0	0	0	0	0	0
^{60}Ni	0	0	0	0	0	0	0	0	0	0	0	0	0	0
^{59}Ni	0	0	0	0	0	0	0	0	0	0	0	0	0	0
^{58}Ni	0	0	0	0	0	0	0	0	0	0	0	0	0	0
^{59}Co	0	0	0	0	0	0	0	0	0	0	0	0	0	0
^{57}Co	0	0	0	0	0	0	0	0	0	0	0	0	0	0
^{58}Fe	0	0	0	0	0	0	0	0	0	0	0	0	0	0
^{57}Fe	0	0	0	0	0	0	0	0	0	0	0	0	0	0
^{56}Fe	0	0	0	0	0	0	0	0	0	0	0	0	0	0
^{55}Fe	0	0	0	0	0	0	0	0	0	0	0	0	0	0
^{54}Fe	0	0	0	0	0	0	0	0	0	0	0	0	0	0
^{55}Mn	0	0	0	0	0	0	0	0	0	0	0	0	0	0
^{54}Mn	0	0	0	0	0	0	0	0	0	0	0	0	0	0
^{53}Mn	0	0	0	0	0	0	0	0	0	0	0	0	0	0
^{54}Cr	0	0	0	0	0	0	0	0	0	0	0	0	0	0
^{53}Cr	0	111.1	0	0	0	0	0	0	0	0	0	0	0	0
^{52}Cr	90.4	32.6	108.0	0	0	0	0	0	0	0	0	0	0	0
^{51}Cr	63.0	5.0	21.2	65.7	0	0	0	0	0	0	0	0	0	0
^{50}Cr	29.9	1.6	4.2	17.3	51.0	0	0	0	0	0	0	0	0	0
^{51}V	12.8	25.3	19.1	34.4	0	0	0	0	0	0	0	0	0	0
^{50}V	20.4	32.8	36.2	35.2	37.9	0	75.3	0	0	0	0	0	0	0
^{49}V	42.5	19.3	29.9	43.0	60.2	79.4	23.6	68.8	0	0	0	0	0	0
^{50}Ti	0.4	9.2	4.5	3.1	0	0	37.8	0	0	0	0	0	0	0
^{49}Ti	4.6	27.2	20.3	12.5	12.1	0	25.6	42.0	0	110.6	0	0	0	0
^{48}Ti	46.3	39.8	48.9	54.8	52.1	64.3	50.5	64.7	100.2	37.6	108.2	0	0	0
^{47}Ti	47.6	27.7	38.0	50.0	54.3	46.6	44.3	57.9	83.0	29.6	43.9	105.7	0	0
^{46}Ti	40.8	26.8	31.5	39.5	47.9	47.4	38.8	47.7	58.8	38.3	42.2	56.1	99.2	0
^{44}Ti	1.2	0.0	0.1	0.4	1.3	3.4	0.1	0.3	1.3	0.0	0.1	0.3	2.8	11.5
^{45}Sc	36.7	30.1	33.7	38.5	43.8	42.5	38.4	45.2	52.3	35.2	42.2	51.5	80.5	89.9

TABLE 6

COSMIC-RAY SOURCE COMPOSITION

Ratio	Derived Value	Solar[a]
$^{44}Ti/^{56}Fe$	<0.0040	0
$^{46}Ti/^{56}Fe$	~0[b]	0.00024
$^{47}Ti/^{56}Fe$	<0.0030	0.00022
$^{48}Ti/^{56}Fe$	<0.020	0.0021
$^{49}Ti/^{56}Fe$	~0[b]	0.00016
$^{50}Ti/^{56}Fe$	0.0084 (+0.0044, −0.0037)	0.00015
$^{49}V/^{56}Fe$	~0[b]	0
$^{50}V/^{56}Fe$	<0.010	0.0000009
$^{51}V/^{56}Fe$	0.0083 (+0.0065, −0.0058)	0.00035
$^{50}Cr/^{56}Fe$	0.0115 (+0.0099, −0.0080)	0.00071
$^{51}Cr/^{56}Fe$	<0.0071	0
$^{52}Cr/^{56}Fe$	0.021 (+0.011, −0.011)	0.014
$^{53}Cr/^{56}Fe$	<0.0089	0.0016
$^{54}Cr/^{56}Fe$	<0.0038	0.00039
$^{53}Mn/^{56}Fe$	<0.013	0
$^{54}Mn/^{56}Fe$	<0.036[c]	0
$^{55}Mn/^{56}Fe$	0.025 (+0.010, −0.010)	0.012
$^{54}Fe/^{56}Fe$	0.046 (+0.020, −0.020)	0.063
$^{55}Fe/^{56}Fe$	<0.039	0
$^{57}Fe/^{56}Fe$	<0.082	0.023
$^{58}Fe/^{56}Fe$	<0.032	0.0032
$^{57}Co/^{56}Fe$	<0.0035	0
$^{59}Co/^{56}Fe$	0.0061 (+0.0022, −0.0030)	0.0027
$^{58}Ni/^{56}Fe$	0.0261 (+0.0066, −0.0063)	0.0408
$^{59}Ni/^{56}Fe$	<0.011	0
$^{60}Ni/^{56}Fe$	0.0280 (+0.0079, −0.0076)	0.0156
$^{61}Ni/^{56}Fe$	<0.0041	0.00067
$^{62}Ni/^{56}Fe$	<0.0063	0.0021
$^{59}Ni/^{58}Ni$	<0.42	0
$^{60}Ni/^{58}Ni$	1.07 (+0.41, −0.39)	0.382
$^{61}Ni/^{58}Ni$	<0.16	0.017
$^{62}Ni/^{58}Ni$	<0.24	0.053
Sc/Fe	<0.005	0.00004
Ti/Fe	<0.007	0.0027
V/Fe	<0.005	0.00033
Cr/Fe	0.0229 (+0.0072, −0.0066)	0.0150
Mn/Fe	0.0225 (+0.0090, −0.0090)	0.0106
Co/Fe	0.0053 (+0.0020, −0.0014)	0.0025
Ni/Fe	0.0545 (+0.0045, −0.0039)	0.0543

[a] Grevesse & Anders 1989; Anders & Ebihara 1982.
[b] Best-fit value negative by slightly more than 1 σ.
[c] Assuming $\tau_{esc}/T_{\beta^-}(^{54}Mn) = 110$.

the sense that most of the Ni is in the form of ^{58}Ni and ^{60}Ni, both of which we determine to be present in the source with values ~4 σ greater than zero. We find, however, that the $^{60}Ni/^{58}Ni$ ratio is enhanced by a factor of 2.8 ± 1.0 over the solar system value. Young et al. (1981) reported a similar enhancement, and while the value found by Tarlé et al. (1979) is not inconsistent with such an enhancement, it also does not rule out the solar value. Examining the abundances of the individual Ni isotopes relative to ^{56}Fe, we see that our data indicate that $^{60}Ni/^{56}Fe$ is enhanced by a factor of 1.8 ± 0.5 relative to solar, while the $^{58}Ni/^{56}Fe$ ratio is actually less than the solar value by a factor of 1.6 ± 0.3, with the absolute amount of ^{60}Ni excess numerically equal (within rather large uncertainties) to the amount of ^{58}Ni depletion. A similar pattern of enhanced ^{60}Ni and depleted ^{58}Ni, with lower significance, was noted by Young et al. (1981). Such a trend might be explained within the context of the simple model of nuclear statistical equilibrium nucleosynthesis of Hainebach et al. (1974) by production in an environment of relatively high neutron excess compared to that in which most of the solar system material was synthesized, with a zone where $\eta \simeq 0.07 \pm 0.01$ reasonably consistent with our Ni data. No

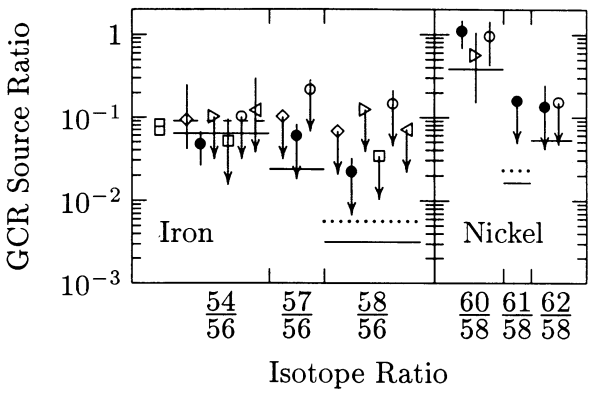

FIG. 9.—Derived relative abundances at the Galactic cosmic-ray source for Fe and Ni isotopes. Shown for comparison are the solar system abundances (Anders & Ebihara 1982, *solid lines*), as well as predicted enhancements in the cosmic ray source based on the Wolf-Rayet model (Prantzos et al. 1985, *dotted lines*), and the supermetallicity model (Woosley & Weaver 1981, *dashed line*). Data points are displayed in order of increasing measurement energy. Symbols and references for the data are the same as in Figure 8, with errors shown as adjusted by Mewaldt (1989). The rectangular box at the left of the $^{54}Fe/^{56}Fe$ measurements shows the value and error range for the $^{54}Fe/^{56}Fe$ ratio that we would obtain if ^{54}Mn were assumed stable in the propagation calculations, to facilitate comparison with the other results which were presumably obtained under the same assumptions.

single zone, however, reproduces the nearly equal abundances of ^{58}Ni and ^{60}Ni we observe without overproducing both species with respect to ^{56}Fe.

The derived source abundance of the ec isotope ^{59}Ni is found to be consistent with zero, however the upper limit of $^{59}Ni/^{58}Ni < 0.42$ is rather high. Even if the solar system abundance of ^{59}Co (Anders & Ebihara 1982; Grevesse & Anders 1989), the daughter of ^{59}Ni decay, were present at the source in undecayed form as ^{59}Ni, the $^{59}Ni/^{58}Ni$ source ratio would only be 0.067. Therefore we are unable to determine, from the measured ^{59}Ni abundance, whether any ^{59}Ni decay has taken place prior to acceleration (however, see § 5.2.2 for evidence based on the abundance of the daughter nuclide). For the

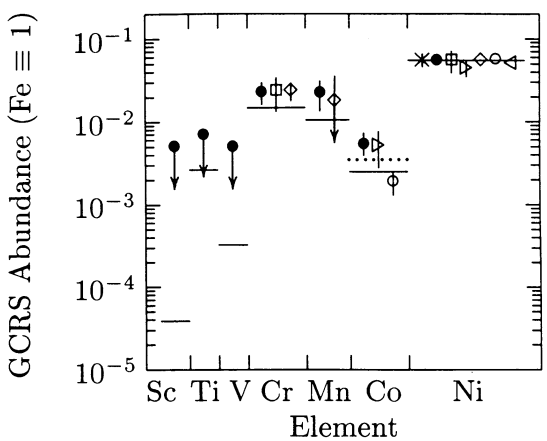

FIG. 10.—Derived relative elemental abundances at the Galactic cosmic-ray source. Horizontal lines indicate the solar system abundances (Grevesse & Anders 1989), and the dotted line shows the abundance predicted by the Wolf-Rayet model (Prantzos et al. 1985). References for the data are the following: (*filled circle*) this work; (×) Garcia-Munoz & Simpson (1979); (*square*) Webber (1982); (*triangle with point right*) Dwyer & Meyer (1985); (*diamond*) Mewaldt & Webber (1990); (*open circle*) Engelmann et al. (1990); (*triangle with point left*) Binns et al. (1981).

heavier Ni isotopes we also have only upper limits on source abundances. The values of ^{61}Ni/^{58}Ni and ^{62}Ni/^{58}Ni are no greater than $\sim$10 and 5 times their solar system values, respectively. Measurements with much better statistics and resolution would be needed to test the prediction of the Wolf-Rayet (W-R) model (Prantzos et al. 1985) of an enhancement of ^{61}Ni/^{58}Ni by a factor of 1.4 over solar.

5.2.2. *Cobalt*

Our elemental ratio of Co/Fe at the source, $0.0053^{+0.0020}_{-0.0014}$, is $2.1^{+0.8}_{-0.6}$ times the solar value. This is considerably higher than the value of 0.0019 ± 0.0006 derived from the *HEAO 3* C2 measurements (Engelmann et al. 1990) and reflects the fact that our measured value at 1 AU is a factor of 1.7 higher than theirs. As illustrated in Figure 10, an enhancement in the cosmic-ray Co abundance by a factor of 1.4 is predicted by the Wolf-Rayet model of Prantzos et al. (1985), assuming that the contribution from the winds of W-R stars is diluted by enough "normal" material to account for the observed ^{22}Ne excess, and that the dilution factor for high-FIP elements such as Ne is the same as that for low-FIP elements such as Co (Meyer 1985a; Prantzos, Arnould, & Arcoragi 1987).

The Co and Ni abundances can be used to address the question of the value of the time delay δt between nucleosynthesis and cosmic-ray acceleration. If iron-group cosmic-ray nuclei are created by nucleosynthesis processes similar to those responsible for the production of the solar system material (Hainebach et al. 1974; Truran 1992), Co isotopes would be produced initially as radioactive isotopes of Ni or higher Z elements. The isotopes ^{57}Ni ($T_{1/2}$ = 36 hr), ^{57}Co ($T_{1/2}$ = 0.74 yr), and ^{59}Ni ($T_{1/2} = 7.5 \times 10^4$ yr) decay only by the process of electron capture. Once accelerated and fully stripped, these species are stable and their relative abundances are frozen at those prevailing at time δt, subject only to further modification by propagation. The variation of the Ni and Co elemental and isotopic source abundances with δt is illustrated by Soutoul et al. (1978).

Previous attempts to use Co to determine δt have been limited to elemental measurements. Koch-Miramond (1981) interpreted the measured *HEAO 3* C2 value as evidence for a long delay time ($\gtrsim 10^5$ yr), while Webber & Gupta (1990), using new cross sections, concluded from the same data set that the arriving Co may be almost purely secondary, with little or no component of primary Co, and estimate that $4 < \delta t < 3 \times 10^4$ yr. Based on this time delay, these authors predict that the isotopic ratio should be ^{59}Co/^{57}Co $\simeq$ 0.43 as opposed to the value of 0.93 we expect at our measurement energy if the delay time is long and the Co/Ni source ratio is the same as that found in solar system material. Clearly the best way to resolve the ambiguity in interpreting the Co abundance data is to make measurements of the Co isotopic composition.

We find that the ratio of ^{59}Co/^{57}Co in the arriving cosmic rays is $2.2^{+2.4}_{-1.4}$, a factor of $5.1^{+5.6}_{-3.3}$ above that predicted by Webber & Gupta (1990) based on their assumption that all the Co is secondary. Our propagation calculation shows that the abundance ratio ^{59}Co/^{56}Fe at the source differs from zero by 2 σ, while the ^{57}Co abundance is consistent with zero. Therefore, while we have no direct evidence for the decay of ^{59}Ni, we do have direct measurements showing that ^{59}Co is present in the arriving cosmic rays, with an abundance too great to be purely secondary. If the production of mass 59 species in the cosmic-ray source material occurred by a process similar to that which reproduces solar system abundances, the presence of significant amounts of ^{59}Co can only mean that $\delta t \gtrsim 10^5$ yr, since the synthesized mass 59 species (^{59}Cu or ^{59}Zn, Truran 1992) must have decayed through ^{59}Ni. Such a delay would lend support to the idea that cosmic rays represent an accelerated sample of interstellar matter or coronal material from cool stars (Meyer 1985b), rather than directly accelerated ejecta of supernovae. Of course, if synthesis takes place by some different process in which ^{59}Co is directly produced, no information on delay times can be deduced from a measurement of the ^{59}Co abundance. A precise determination of the ^{59}Ni abundance should help to clarify the situation.

5.2.3. *Iron and Manganese*

As shown in Figure 9, we obtain only upper limits for the abundances of the heavier Fe isotopes ^{57}Fe and ^{58}Fe. Our limits are comparable to the best previously reported (Mewaldt et al. 1980; Webber 1981) and allow for possible enhancements over the solar system values by factors of up to 3.5 and 10 for ^{57}Fe/^{56}Fe and ^{58}Fe/^{56}Fe, respectively. As was the case for ^{61}Ni, a predicted enhancement of ^{58}Fe/^{56}Fe by a factor of 1.8 over solar following from the Wolf-Rayet model (Prantzos et al. 1985) is beyond our limit of detection. Our inferred source abundance of the ec species ^{55}Fe is consistent with zero.

The determination of the ^{54}Fe source abundance depends critically on evaluating how much of the observed ^{54}Fe was produced as the daughter of ^{54}Mn β^- decay (Grove et al. 1991). This assessment is difficult since the half-life T_{β^-}(^{54}Mn) for the β^- decay of ^{54}Mn is very poorly known. In the laboratory, ^{54}Mn decays predominantly by electron capture with a half-life of 312 days. When stripped of its orbital electrons as in cosmic rays, decay is still energetically possible by both β^- and β^+ branches. The β^- branch is expected to dominate, with a partial half-life estimated on theoretical grounds by Cassé (1973) to be within a factor of 2 of 2 Myr, although Wilson (1978) states that the actual uncertainties are larger, with values from 0.065 to 9.8 Myr possible. Sur et al. (1989) measure a lower limit for T_{β^+} of 2×10^7 yr, from which they infer a lower limit of 4×10^4 yr for T_{β^-}.

The uncertainty in the value of T_{β^-} presently prevents the use of ^{54}Mn as an absolute chronometer for measuring the mean escape time, τ_{esc}, of iron-group cosmic rays from the Galaxy (Cassé 1973), and has led to some disagreement over whether ^{54}Mn decays to any extent during propagation. Koch et al. (1981) reported that the flatness of the Mn/Fe elemental abundance ratio as a function of energy as measured by *HEAO 3* C2 suggested the decay of ^{54}Mn with a half-life of $\simeq$1–2 Myr, however, using different cross sections with the same data set, Ormes & Protheroe (1981) concluded that there is no evidence for any ^{54}Mn decay. In both cases, the assumption was made that the Mn/Fe source ratio is similar to that of solar system material (Mewaldt 1981). Taking into account the uncertainties in both the Mn source abundance and T_{β^-}(^{54}Mn), Grove et al. (1991) demonstrated that presently available measurements of elemental ratios do not provide enough information to decide whether ^{54}Mn decays or not, and conclude that isotopic measurements are necessary to resolve the question. As shown in Figure 8, our upper limit for ^{54}Mn/^{53}Mn at 1 AU is a factor of 3.7 below the ratio expected if ^{54}Mn were stable, indicating that most of the ^{54}Mn arriving at 325 MeV per nucleon has in fact decayed.

To study the effect of the decay of ^{54}Mn on the arriving

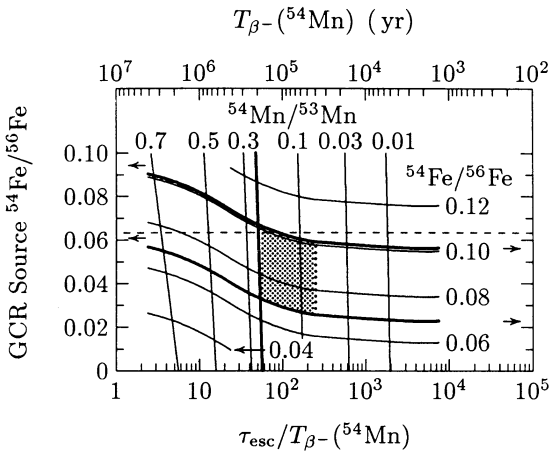

FIG. 11.—Contour plot of the values of the ratios $^{54}Fe/^{56}Fe$ and $^{54}Mn/^{53}Mn$ expected to be measured at 325 MeV per nucleon at Earth as functions of the source $^{54}Fe/^{56}Fe$ abundance ratio (*ordinate*) and ratio of the mean escape time τ_{esc} to the half-life for the β^- decay of ^{54}Mn, $T_{\beta^-}(^{54}Mn)$ (*bottom abscissa*), assuming the solar value of the $^{55}Mn/^{56}Fe$ ratio at the source. Across the top abscissa are values of the ^{54}Mn half-life scaled from the ratios on the bottom abscissa assuming $\tau_{esc} = 10$ Myr. Contours corresponding to measured limits on the plotted abundance ratio are shown as heavy solid lines. Arrows at the left and right axes indicate asymptotic values of the source $^{54}Fe/^{56}Fe$ ratio for the limiting $^{54}Fe/^{56}Fe$ contours as $\tau_{esc}/T_{\beta^-} \to 0$ (*left*) and $\tau_{esc}/T_{\beta^-} \to \infty$ (*right*). The shaded area shows the region allowed by the intersection of our measured limits and by the lower limit for the ^{54}Mn half-life (*dotted line*) obtained by Sur et al. (1989). The dashed line indicates the solar value of the $^{54}Fe/^{56}Fe$ ratio.

abundances of mass 54 species, we calculated the expected relative abundances at 1 AU of $^{54}Mn/^{53}Mn$ and $^{54}Fe/^{56}Fe$ for a range of assumed values of the $^{54}Fe/^{56}Fe$ source abundance ratio and $T_{\beta^-}(^{54}Mn)$. A contour plot displaying the results of these calculations is shown in Figure 11 (based on Leske et al. 1992). By plotting the results in terms of τ_{esc}/T_{β^-} our conclusions become independent of the choice of the density n_H of the ISM. Across the top abscissa we show the corresponding values of T_{β^-} scaled from the ratios on the lower axis assuming $\tau_{esc} = 10$ Myr (Wiedenbeck & Greiner 1980). We see that for any given value of the $^{54}Fe/^{56}Fe$ source abundance ratio, the value of $^{54}Fe/^{56}Fe$ expected in the arriving cosmic rays varies by ~ 0.035 depending on whether ^{54}Mn is stable or decays completely into ^{54}Fe, adding $\sim \frac{1}{3}$ the Mn abundance (which in turn is ~ 0.1 of the Fe abundance) to ^{54}Fe in the process. Also, for any value of τ_{esc}/T_{β^-}, the expected value of arriving $^{54}Fe/^{56}Fe$ varies linearly with the source value of this ratio. The expected value of $^{54}Mn/^{53}Mn$ depends mainly on the value of T_{β^-}. Contours corresponding to our measurements of the upper and lower limits of the $^{54}Fe/^{56}Fe$ ratio and our upper limit on the $^{54}Mn/^{53}Mn$ ratio are indicated by heavy solid lines, and the 4×10^4 yr lower limit on $T_{\beta^-}(^{54}Mn)$ obtained by Sur et al. (1989) is indicated by the dotted line. The allowed region of the plot resulting from the intersection of these measured limits is shown by the shaded area. Note that the location of the right boundary of the region (obtained from the lower limit on T_{β^-}) depends on the scale on the top abscissa, which is based on the assumption that $\tau_{esc} = 10$ Myr. Dropping this limit, however, has negligible effect on our inferred value of the $^{54}Fe/^{56}Fe$ source abundance ratio, since the Fe isotope contours become essentially horizontal towards lower T_{β^-}. (The asymptotic values of the limiting $^{54}Fe/^{56}Fe$ measurement contours as $T_{\beta^-} \to \infty$ and $T_{\beta^-} \to 0$ are indicated by arrows at the left and right axes, respectively).

From Figure 11, we see that a source value of $^{54}Fe/^{56}Fe = 0.046 \pm 0.020$ is consistent with both our $^{54}Fe/^{56}Fe$ measurement and the amount of ^{54}Mn observed to decay. This value is less than one standard deviation below the solar system value of 0.063 (Anders & Ebihara 1982), shown by a dashed line in the figure. Although our value appears somewhat low compared to other values indicated in Figure 9, note that the earlier results do not include corrections for ^{54}Mn decay since the extent of such decay was unknown. If one assumed ^{54}Mn was stable, Figure 11 indicates that our source value for $^{54}Fe/^{56}Fe$ would change to 0.077 ± 0.017. This value is shown as a rectangular box at the left side of Figure 9 to facilitate comparison with the other results. While consistent with the solar value, our $^{54}Fe/^{56}Fe$ ratio is a factor of 1.95 (2.2 σ) lower than that predicted by the supermetallicity model of Woosley & Weaver (1981), shown by a dashed line in Figure 9.

Based on our upper limit of $^{54}Mn/^{53}Mn < 0.25$ and the results shown in Figure 11, we find that $\tau_{esc} > 50 T_{\beta^-}(^{54}Mn)$. If one accepts the value $T_{\beta^-} > 4 \times 10^4$ yr (Sur et al. 1989), we conclude that $\tau_{esc} > 2$ Myr for iron-group cosmic rays. In Table 7 we compare our determination of τ_{esc} with those found by other investigators using different radioactive isotopes. There is no indication that τ_{esc} varies for different species, although the uncertainties on these derived values are large. For the other Mn secondary, we find that the source abundance of the ec isotope ^{53}Mn is consistent with zero, as expected.

The $^{55}Mn/^{56}Fe$ source abundance ratio may be better determined by making use of the measured Mn/Fe ratio along with the $^{55}Mn/^{53}Mn$ ratio, due to the better statistics and smaller uncertainties of the elemental measurement. The elemental ratio, however, is dependent on the ^{54}Mn half-life in a manner illustrated in Figure 12. Here we show contours of the expected values of $^{55}Mn/^{53}Mn$, $^{54}Mn/^{53}Mn$, and Mn/Fe in the arriving cosmic rays at 325 MeV per nucleon for a range of values for the $^{55}Mn/^{56}Fe$ source ratio and $\tau_{esc}/T_{\beta^-}(^{54}Mn)$ at the value of the $^{54}Fe/^{56}Fe$ source abundance ratio derived from our data. Calculations show that the value of $^{55}Mn/^{56}Fe$ at the source for a given arriving $^{55}Mn/^{53}Mn$ value decreases by ~ 0.001 if the $^{54}Fe/^{56}Fe$ source ratio is reduced to its lowest allowed value due to the decreasing production of ^{53}Mn from ^{54}Fe,

TABLE 7

COSMIC RAY CONFINEMENT TIME

Isotope	Half-life (Myr)	Confinement Time (Myr)	Reference
^{10}Be	1.6	15 (+7, −4)	Simpson & Garcia-Munoz 1988
		8.4 (+4.0, −2.4)	Wiedenbeck & Greiner 1980
^{26}Al	0.87	9 (+20, −6.5)	Wiedenbeck 1983
^{36}Cl	0.3	>1	Wiedenbeck 1985
^{54}Mn	>0.04	>2	This work

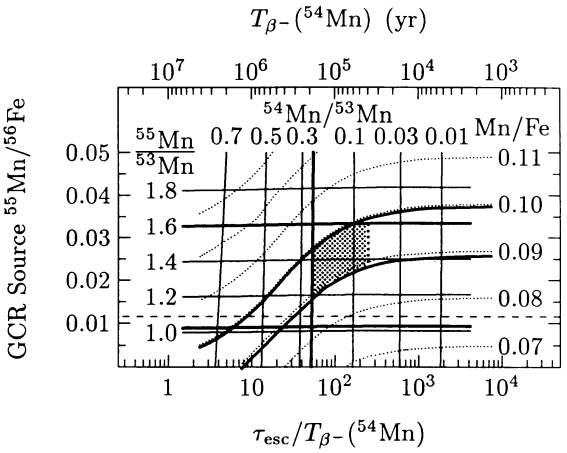

FIG. 12.—Contour plot of the values of the ratios $^{55}\mathrm{Mn}/^{53}\mathrm{Mn}$, $^{54}\mathrm{Mn}/^{53}\mathrm{Mn}$ (*light solid lines*), and Mn/Fe (*light dotted lines*) expected to be measured at 325 MeV per nucleon at Earth as functions of the source $^{55}\mathrm{Mn}/^{56}\mathrm{Fe}$ ratio (*ordinate*) and $\tau_{esc}/T_{\beta^-}(^{54}\mathrm{Mn})$ (*bottom abscissa*) if the $^{54}\mathrm{Fe}/^{56}\mathrm{Fe}$ source abundance ratio is 0.046. The top abscissa shows the $^{54}\mathrm{Mn}$ half-life values if τ_{esc} = 10 Myr. The heavy dotted line marks the 4×10^4 yr lower limit for the $^{54}\mathrm{Mn}$ half-life obtained by Sur et al. (1989). Heavy solid lines indicate contours corresponding to our measured limits on the plotted abundance ratios, with the region of intersection shaded. The dashed horizontal line indicates the solar value of the $^{55}\mathrm{Mn}/^{56}\mathrm{Fe}$ ratio.

with a corresponding increase seen when the $^{54}\mathrm{Fe}/^{56}\mathrm{Fe}$ source ratio is at its highest extreme. The area bounded by the intersection of our measurements of $^{55}\mathrm{Mn}/^{53}\mathrm{Mn}$ and Mn/Fe, and by our limit on the $^{54}\mathrm{Mn}/^{53}\mathrm{Mn}$ value and the lower limit of $T_{\beta^-}(^{54}\mathrm{Mn}) > 4 \times 10^4$ yr is shaded. Once again, the uncertainty in the lower limit of T_{β^-} has no effect on the inferred $^{55}\mathrm{Mn}/^{56}\mathrm{Fe}$ source ratio. From inspection of Figure 12, we see that without using our Mn/Fe elemental measurement, a loose determination of the $^{55}\mathrm{Mn}/^{56}\mathrm{Fe}$ source ratio of 0.021 ± 0.014 may be obtained from our measured $^{55}\mathrm{Mn}/^{53}\mathrm{Mn}$ ratio alone.

The source value of $^{55}\mathrm{Mn}/^{56}\mathrm{Fe}$ consistent with all our measurements is 0.025 ± 0.010, which is 1.3 σ above the solar system value (shown as a dashed horizontal line in the figure) and more nearly approaches the solar value for larger values of T_{β^-}. Our determined value is within the range of Mn/Fe = 0.018 ± 0.018 deduced by Mewaldt & Webber (1990). Our conclusion of an enhanced Mn source abundance and suggestion of a relatively short $^{54}\mathrm{Mn}$ half-life are not inconsistent with other data. We point out that Grove et al. (1991), using a compilation of satellite-based elemental measurements, particularly those of the *HEAO 3* C2 experiment, report that the best fit to the data over a wide range of energies is obtained for $T_{\beta^-}(^{54}\mathrm{Mn}) \sim 10^5$ yr and a Mn/Fe source ratio of ~ 0.03, although they find acceptable fits for all values of $T_{\beta^-} > 4 \times 10^4$ yr and all source abundances of Mn/Fe < 0.03 as well.

5.2.4. *Chromium*

Our derived Cr/Fe elemental source ratio, 0.023 ± 0.007, is in excellent agreement with the value of 0.024 ± 0.006 deduced by Mewaldt & Webber (1990) using a compilation of Cr elemental abundance measurements. Our value is a factor of 1.53 ± 0.47, or only 1.13 standard deviations, above the solar system value.

The measured upper limit of the $^{54}\mathrm{Cr}$ isotopic fraction in the arriving cosmic rays (Table 3) is consistent with that expected due to secondary production, mainly from Fe. Note that if all the missing $^{54}\mathrm{Mn}$ had decayed to $^{54}\mathrm{Cr}$, we would expect to find

$$^{54}\mathrm{Cr}/\mathrm{Cr} \simeq 0.73 \times (^{54}\mathrm{Mn}/\mathrm{Mn})_{\text{no decay}} \times (\mathrm{Mn}/\mathrm{Cr}) \simeq 0.13$$

due to this decay alone, which is a factor of 2.6 greater than the upper limit of 0.052 we observe and more than 6 times greater than the possible excess over the expected value of 0.03. We therefore conclude that the bulk of the $^{54}\mathrm{Mn}$ decay occurs via the β^- branch to $^{54}\mathrm{Fe}$ as we implicitly assumed, and not via β^+ or ec decay to $^{54}\mathrm{Cr}$.

While a slight gap appears in the Cr distribution near mass 51 (Fig. 7), its significance is marginal at best, and analysis shows that the abundance of the ec species $^{51}\mathrm{Cr}$ is consistent with that expected for production by spallation. We can not confirm the slight "dip" suggested by the data of Tarlé et al. (1979).

The derived source abundance ratio $^{52}\mathrm{Cr}/^{56}\mathrm{Fe} = 0.021 \pm 0.011$ is consistent with the solar system value of 0.014 (Anders & Ebihara 1982) and differs from zero by 1.9 standard deviations. In the context of the nuclear statistical equilibrium calculations of Hainebach et al. (1974), this value rules out zones with $\eta \gtrsim 0.05$ as the site for most of the cosmic-ray nucleosynthesis, which would limit the fraction of material contributed from such high-η zones. A more sophisticated model is probably required to explain both our Cr and Ni observations. Our data (Table 6) also suggest that $^{50}\mathrm{Cr}$ may be present at the source, although the significance of the determination is only 1.3 σ.

5.2.5. *Vanadium, Titanium, and Scandium*

Our measured vanadium mass fractions (Fig. 8) are all within 2 standard deviations of those expected from secondary production. The apparently low abundance of $^{49}\mathrm{V}$ found by Webber (1981) has been used to argue in favor of the distributed acceleration of cosmic rays (Silberberg et al. 1983), in which cosmic rays continue to be accelerated during propagation by collisions with widely distributed, weak shocks of somewhat dissipated supernova remnants. If reacceleration occurs, particles would have spent a considerable amount of time at energies much lower than those at which they are observed. As a result, the abundances of ec species could be significantly reduced due to the rapid increase in the electron attachment cross sections with decreasing energy (Raisbeck & Yiou 1976). In the simple model of Silberberg et al. (1983), a fivefold increase in the interstellar energy of particles arriving at 1 AU at 600 to 800 MeV per nucleon resulted in a decrease by a factor of 2 in the expected abundances of $^{49}\mathrm{V}$ and $^{51}\mathrm{Cr}$. Since, according to these authors, an even greater decrease would be expected at the lower energy of 325 MeV per nucleon of our measurements, even allowing for the increase in production cross sections at low energy, our data suggest that reacceleration of this magnitude is unlikely. Although the maximum amount of $^{51}\mathrm{Cr}$ decay permitted by our measurements (at the 1 σ level) is 30% of that expected to be produced, which is sufficient to account for the apparent excess of $^{51}\mathrm{V}$ we observe, the decreased $^{49}\mathrm{V}$ abundance is not accompanied by an increase in $^{49}\mathrm{Ti}$. We find that the decay of no more than $\sim 30\%$ of the initial $^{49}\mathrm{V}$ would produce all the $^{49}\mathrm{Ti}$ we observe, which is even somewhat lower than expected from iron spallation alone. In principle, the slight skew observed in the V mass fraction pattern may be caused by systematic effects, such as employing peak shapes that may be too narrow, or shifting the mass scale downward by ~ 0.15 amu, however

such a shift is rather large and in the opposite direction of that expected from free-parameter fits to the V distribution (Fig. 3). We have no indication that such systematic effects exist, but unless these possibilites can be completely ruled out, one cannot assign any great significance to the small discrepancies observed in the V mass fractions. More quantitative statements as to the amount of reacceleration permitted by our observations would require detailed propagation calculations within the framework of a reacceleration model, which we have not performed. Our derived limit on the V/Fe elemental ratio at the source, 0.005, is still a factor of ~ 15 greater than the solar system value.

Our measured Ti mass fractions (Fig. 8) are in remarkably good agreement with the values predicted by our propagation model. This is probably due largely to the reliability of the new fragmentation cross sections of Webber et al. (1990b, c, d) which are measured to an accuracy of $\pm 1.5\%$ for production of the dominant Ti masses (46, 47, and 48) down to $\pm 10\%$ for the production of ^{50}Ti from the spallation of ^{56}Fe.

One notable exception to the agreement between theory and experiment is the case of ^{50}Ti, for which our measured mass fraction is 2.4 σ greater than expected. While the statistical errors are larger, the measurement of Webber (1981) is similarly high. Our observed mass histogram (Fig. 7) shows that our high ^{50}Ti value is associated with a well-defined peak and is not due primarily to uncertainties in the derived peak shape, as may be the case for apparent excesses of ^{57}Fe, ^{58}Fe, and ^{51}V. Similarly, spillover from V can be ruled out (Fig. 5, *bottom*). Assuming the validity of the measured cross sections, the unmeasured production cross sections obtained from the formulae would have to be in error by more than an order of magnitude to account for our results. If so, it is somewhat surprising that similar discrepancies are not found for other Ti isotopes.

We find that the total Ti/Fe source elemental abundance ratio is less than 0.007, which is a factor of ~ 2.6 greater than the solar system value. Individual isotope abundances are consistent with zero, again with the exception of the derived value of ^{50}Ti/^{56}Fe, which is 2.3 σ above zero and a factor of 56 ± 30 above the solar value. If real, this would be a cosmic-ray source isotopic anomaly of unprecedented proportions. The nucleosynthesis of ^{50}Ti is not well understood. It is not expected to be produced in significant quantites by explosive nucleosynthesis (Woosley et al. 1973; Truran 1992). Calculations show the ^{50}Ti abundance is not greatly enhanced in neutron-capture reactions (Lamb et al. 1977), and may require a very neutron-rich environment to form (Hainebach et al. 1974). Under such conditions, large enhancements of ^{54}Cr and ^{58}Fe would also be expected, which cannot be ruled out by our measurements. At present it is unclear whether our ^{50}Ti measurement should be attributed to large cross section errors or large ^{50}Ti source abundances. It should be possible to confirm or refute the measurement within the next few years as results become available from new high-resolution isotope detectors. If confirmed, the ^{50}Ti production and destruction cross sections that are not yet determined should be measured to reduce the uncertainty in the interpretation of this puzzling observation.

The element Sc has only one stable isotope, ^{45}Sc. Our observed mass distribution (Fig. 7), while based on low statistics, shows that the observed Sc events are consistent with identification as this isotope. Scandium has a very low abundance in solar system material, being only 3.8×10^{-5} times as abundant as Fe (Grevesse & Anders 1989). Our measured arriving abundance is entirely consistent with that expected for a secondary origin for Sc, while our limit on the inferred source abundance ratio, Sc/Fe < 0.005, is a factor of ~ 130 greater than the solar system value.

6. SUMMARY

Our analysis of the iron-group cosmic rays shows that the source composition of these particles, for species where we can make such a determination, generally does not differ greatly from that of solar system material. The largest discrepancy is that of the ^{60}Ni/^{58}Ni ratio, which is 2.8 ± 1.0 times greater than its solar system value. This enhancement is found to be associated with both a depletion of the ^{58}Ni abundance and an enhancement of the ^{60}Ni abundance relative to solar, neither of which is predicted by models proposed to explain isotopic anomalies observed for lighter elements. The Co/Fe abundance ratio appears to be enhanced by a factor of $2.1^{+0.8}_{-0.6}$ and is marginally consistent with the most extreme enhancement predicted by the Wolf-Rayet model of Prantzos et al. (1985), however this is a low statistics measurement and in disagreement with that reported by other investigators. The isotopic ratio ^{54}Fe/^{56}Fe is consistent with its solar value, with a slightly lower abundance being favored, and is 2.2 σ below the abundance expected from the supermetallicity model of Woosley & Weaver (1981). We find that the ratio ^{55}Mn/^{56}Fe is a factor of 2.1 ± 0.8 greater than the solar value. The source value of the Cr/Fe elemental ratio appears to be marginally greater than solar, with an enhancement of 1.53 ± 0.47. We find that ^{52}Cr is present in the source, with an abundance relative to ^{56}Fe that is consistent with its solar value. Any V, Ti, or Sc in the source is not detectable in the elemental measurements, with values that must be well below 1% of the Fe source abundance. An apparently high value of the ^{50}Ti abundance deserves further attention, but the significance of this measurement and its proper interpretation are unclear at the present time.

The amount of ^{59}Co we observe in the arriving cosmic rays suggests that this isotope is present in the source. If not synthesized directly but rather produced as the daughter of the ec decay of ^{59}Ni, as is widely believed to have been the case for production of the solar system material, the presence of ^{59}Co indicates that a time delay of $\gtrsim 10^5$ yr exists between the synthesis of iron-group species and their acceleration to cosmic-ray energies. We do not have a corroborating measurement of a low ^{59}Ni abundance, however, due to insufficient resolution and statistics; therefore the possibility remains open for a different synthesis mechanism for the observed ^{59}Co which might invalidate the conclusion of a long time delay.

We do observe that most of the ^{54}Mn ($\sim \frac{3}{4}$ of that expected to be produced) has decayed as measured at 325 MeV per nucleon at Earth (corresponding to ~ 700 MeV per nucleon in interstellar space). Given the lower limit of 4×10^4 yr for the half-life of the β^- decay of ^{54}Mn (Sur et al. 1989), our measurements show that the confinement time for iron-group cosmic rays is at least 2 Myr. Better laboratory measurements of the ^{54}Mn β^- half-life would allow us to further restrict the value of the confinement time. Previous low energy determinations of the ^{54}Fe source abundance should be reinterpreted in light of this new information on the decay of ^{54}Mn.

Our measurements of the abundances of the ec isotopes ^{51}Cr and ^{49}V may help to set new limits on the amount of reacceleration that takes place if properly interpreted in the framework of a reacceleration model. Reacceleration is not required to explain our results, however, as the abundances of all ec

species and their daughters are within 2 σ of those predicted by the standard leaky box model.

The author wishes to thank his faculty advisor, Professor Mark Wiedenbeck, for his continual guidance and encouragement throughout this work. We also thank the Heckman/Greiner group at the Lawrence Berkeley Laboratory who designed, constructed, and calibrated the instrument used for this study. We gratefully acknowledge the contributions of Professor William Webber who provided the computer code used for calculating the fragmentation cross sections, and of Professor James Truran for enlightening discussions of recent ideas and results in the field of iron-group nucleosynthesis. This work was supported, in part, by NASA under grants NAG5-308 and NAGW-1982, and by NASA's Graduate Student Researchers Program under grant NGT 14-020-802.

REFERENCES

Anders, E., & Ebihara, M. 1982, Geochim. Cosmochim. Acta, 46, 2363
Andersen, H. H., & Ziegler, J. F. 1977, Hydrogen Stopping Powers and Ranges in All Elements (NY: Pergamon)
Bieser, F. S., Greiner, D. E., Beleal, E., & Aalami, D. D. 1977, Proc. 15th Internat. Cosmic Ray Conf. (Plovdiv), 9, 91
Binns, W. R., Fickle, R. K., Garrard, T. L., Israel, M. H., Klarmann, J., Stone, E.C., & Waddington, C. J. 1981, ApJ, 247, L115
Byrnak, B., Lund, N., Rasmussen, I. L., Rotenberg, M., Engelmann, J., Goret, P., & Juliusson, E. 1983, Proc. 18th Internat. Cosmic Ray Conf. (Bangalore), 2, 29
Cassé, M. 1973, ApJ, 180, 623
Crawford, H. J. 1979, Ph.D. thesis, Univ. California-Berkeley
Dwyer, R., & Meyer, P. 1985, ApJ, 294, 441
———. 1987, ApJ, 322, 981
Engelmann, J. J., et al. 1990, A&A, 233, 96
Ferrando, P., Lal, N., McDonald, F. B., & Webber, W. R. 1991, A&A, 247, 163
Ferrando, P., Webber, W. R., Goret, P., Kish, J. C., Schrier, D. A., Soutoul, A., & Testard, O. 1988, Phys. Rev. C, 37, 1490
Fisk, L. A. 1971, J. Geophys. Res., 76, 221
Garcia-Munoz, M., & Simpson, J. A. 1979, Proc. 16th Internat. Cosmic Ray Conf. (Kyoto), 1, 270
Garcia-Munoz, M., Simpson, J. A., Guzik, T. G., Wefel, J. P., & Margolis, S. H. 1987, ApJS, 64, 269
Goulding, F. S., & Harvey, B. G. 1975, Ann. Rev. Nucl. Sci., 25, 167
Greiner, D. E., Bieser, F. S., Crawford, H., Heckman, H. H., & Lindstrom, P. S. 1977, Proc. 15th Internat. Cosmic Ray Conf. (Plovdiv), 9, 97
Greiner, D. E., Bieser, F. S., & Heckman, H. H. 1978, IEEE Trans. Geosci. Electronics, GE-16, 163
Grevesse, N., & Anders, E. 1989, in AIP Conf. Proc. 183, Cosmic Abundances of Matter, ed. C. J. Waddington (NY: AIP), 1
Grove, J. E., Christian, E. R., Mewaldt, R. A., Schindler, S. M., Stone, E. C., Buffington, A., & Rasmussen, I. L. 1990, Proc. 21st Internat. Cosmic Ray Conf. (Adelaide), 3, 53
Grove, J. E., Hayes, B. T., Mewaldt, R. A., & Webber, W. R. 1991, ApJ, 377, 680
Hainebach, K. L., Clayton, D. D., Arnett, W. D., & Woosley, S. E. 1974, ApJ, 193, 157
Henkel, M., et al. 1990, Proc. 21st Internat. Cosmic Ray Conf. (Adelaide), 3, 15
Hesse, A., et al. 1991, Proc. 22d Internat. Cosmic Ray Conf. (Dublin), 1, 596
Koch, L., et al. 1981, A&A, 102, L9
Koch-Miramond, L. 1981, Proc. 17th Internat. Cosmic Ray Conf. (Paris), 12, 21
Lamb, S. A., Howard, W. M., Truran, J. W., & Iben, I., Jr. 1977, ApJ, 217, 213
Lederer, C. M., & Shirley, V. S., eds. 1978, Table of Isotopes, 7th ed. (NY: Wiley)
Leske, R. A., Milliken, B., & Wiedenbeck, M. E. 1992, ApJ, 390, L99
Leske, R. A., & Wiedenbeck, M. E. 1990, Proc. 21st Internat. Cosmic Ray Conf. (Adelaide), 3, 57
Letaw, J. R., Silberberg, R., & Tsao, C. H. 1983, ApJS, 51, 271
Lezniak, J. A., & Webber, W. R. 1978, ApJ, 223, 676
Lund, N. 1989, in AIP Conf. Proc. 183, Cosmic Abundances of Matter, ed. C. J. Waddington (NY: AIP), 111
Meneguzzi, M., Audouze, J., & Reeves, H. 1971, A&A, 15, 337
Mewaldt, R. A. 1981, Proc. 17th Internat. Cosmic Ray Conf. (Paris), 13, 49
———. 1989, in AIP Conf. Proc. 183, Cosmic Abundances of Matter, ed. C. J. Waddington (NY: AIP), 124
Mewaldt, R. A., Spalding, J. D., Stone, E. C., & Vogt, R. E. 1980, ApJ, 236, L121
Mewaldt, R. A., & Webber, W. R. 1990, Proc. 21st Internat. Cosmic Ray Conf. (Adelaide), 3, 432
Meyer, J.-P. 1985a, Proc. 19th Internat. Cosmic Ray Conf. (La Jolla), 9, 141
———. 1985b, ApJS, 57, 173
———. 1989, in AIP Conf. Proc. 183, Cosmic Abundances of Matter, ed. C. J. Waddington (NY: AIP), 245
Olive, K. A., & Schramm, D. N. 1982, ApJ, 257, 276
Ormes, J. F., & Protheroe, R. J. 1981, Proc. 17th Internat. Cosmic Ray Conf. (Paris), 2, 31
Prantzos, N., Arnould, M., & Arcoragi, J.-P. 1987, ApJ, 315, 209
Prantzos, N., Arnould, M., Arcoragi, J.-P., & Cassé, M. 1985, Proc. 19th Internat. Cosmic Ray Conf. (La Jolla), 3, 167
Pratt, R. H., Ron, A., & Tseng, H. K. 1973, Rev. Mod. Phys., 45, 273
Raisbeck, G. M., & Yiou, F. 1976, in Spallation Nuclear Reactions and Their Applications, ed. B. S. P. Shen & M. Merker (Dordrecht: Reidel), 83
Silberberg, R., Tsao, C. H., Letaw, J. R., & Shapiro, M. M. 1983, Phys. Rev. Lett., 51, 1217
Simpson, J. A. 1983, Ann. Rev. Nucl. Part. Sci., 33, 323
Simpson, J. A., & Garcia-Munoz, M. 1988, Space Sci. Rev., 46, 205
Soutoul, A., Cassé, M., & Juliusson, E. 1978, ApJ, 219, 753
Soutoul, A., Ferrando, P., & Webber, W. R. 1990, Proc. 21st Internat. Cosmic Ray Conf. (Adelaide) 3, 337
Sur, B., Vogel, K. R., Norman, E. B., Lesko, K. T., Larimer, R.-M., & Browne, E. 1989, Phys. Rev. C, 39, 1511
Tang, K. K. 1990, Proc. 21st Internat. Cosmic Ray Conf. (Adelaide), 3, 373
Tarlé, G., Ahlen, S. P., & Cartwright, B. G. 1979, ApJ, 230, 607
Truran, J. W. 1992, private communication
Tueller, J., Love, P. L., Israel, M. H., & Klarmann, J. 1979, ApJ, 228, 582
Vylet, V., Waddington, C. J., Binns, W. R., Garrard, T. L., Israel, M. H., Klarmann, J., & Metzger, M. 1990, Proc. 21st Internat. Cosmic Ray Conf. (Adelaide), 3, 19
Walton, J. T., Sommer, H. A., Greiner, D. E., & Bieser, F. S. 1978, IEEE Trans. Nucl. Sci., NS-25, 391
Webber, W. R. 1981, Proc. 17th Internat. Cosmic Ray Conf. (Paris), 2, 80
———. 1982, ApJ, 255, 329
———. 1991, private communication
Webber, W. R., & Gupta, M. 1990, ApJ, 348, 608
Webber, W. R., Kish, J. C., & Schrier, D. A. 1990a, Phys. Rev. C, 41, 520
———. 1990b, Phys. Rev. C, 41, 533
———. 1990c, Phys. Rev. C, 41, 547
———. 1990d, Phys. Rev. C, 41, 566
Westfall, G. D., Wilson, L. W., Lindstrom, P. J., Crawford, H. J., Greiner, D. E., & Heckman, H. H. 1979, Phys. Rev. C, 19, 1309
Wiedenbeck, M. E. 1983, Proc. 18th Internat. Cosmic Ray Conf. (Bangalore), 9, 147
———. 1985, Proc. 19th Internat. Cosmic Ray Conf. (La Jolla), 2, 84
———. 1990, Proc. 21st Internat. Cosmic Ray Conf. (Adelaide), 11, 57
Wiedenbeck, M. E., & Greiner, D. E. 1980, ApJ, 239, L139
Wilson, L. W. 1978, Ph.D. thesis, Univ. California-Berkeley
Woosley, S. E., Arnett, W. D., & Clayton, D. D. 1973, ApJS, 26, 231
Woosley, S. E., & Weaver, T. A. 1981, ApJ, 243, 651
Young, J. S., Freier, P. S., Waddington, C. J., & Brewster, N. R. 1981, ApJ, 246, 1014
Ziegler, J. F. 1980, Handbook of Stopping Cross-Sections for Energetic Ions in All Elements (NY: Pergamon)